Summer 2017

Study of Multiferroic Properties of Ferroelectric- Ferromagnetic Heterostructures BZT-BCT/LSMO

Md Abdullah-Al Mamun
Missouri State University, Mamun113@live.missouristate.edu

STUDY OF MULTIFERROIC PROPERTIES OF FERROELECTRIC-FERROMAGNETIC HETEROSTRUCTURES BZT-BCT/LSMO

A Masters Thesis

Presented to

The Graduate College of

Missouri State University

In Partial Fulfillment

Of the Requirements for the Degree

Master of Science, Materials Science

By

Md Abdullah-Al Mamun

August 2017

STUDY OF MULTIFERROIC PROPERTIES OF FERROELECTRIC-FERROMAGNETIC HETEROSTRUCTURES BZT-BCT/LSMO

Physics, Astronomy, and Materials Science

Missouri State University, August 2017

Master of Science

Md Abdullah-Al Mamun

ABSTRACT

Currently, there has been a flurry of research focused on multiferroic materials due to their potential applications. Lead (Pb)-based ferroelectric and multiferroic materials (PZT, PMN-PT, PZN-PT etc.) have been widely used for sensors, actuators, and electro-mechanical applications due to their excellent dielectric and piezoelectric properties. However, these materials are facing global restriction due to the toxicity of Pb. In this thesis, multiferroic properties of ferroelectric-ferromagnetic heterostructures consist of Pb-free perovskite oxides $0.5Ba(Zr_{0.2}Ti_{0.8})O_3$-0.5 $(Ba_{0.7}\ Ca_{0.3})TiO_3$ (BZT-BCT) and $La_{0.7}Sr_{0.3}MnO_3$ (LSMO) have been studied. The heterostructures BZT-BCT/LSMO were fabricated on $LaAlO_3$ (LAO) and Pt substrates by pulsed laser deposition. Structural and crystalline qualities of the films have been investigated through theta-2theta scan, rocking curve, and phi-scan of X-Ray diffraction (XRD) and Raman spectroscopy. Ferroelectric and ferromagnetic properties have been characterized using the Sawyer-Tower method, a SQUID magnetometer, and Ferromagnetic resonance (FMR) spectroscopy. A well-behaved magnetization-magnetic field (M-H) hysteresis has been observed in LSMO as well as heterostructures, indicating ferromagnetism in the films. FMR spectroscopy data support the static magnetization data obtained using SQUID. These results may guide the development of next-generation lead-free ferroelectric-ferromagnetic heterostructures for magnetoelectric device applications.

KEYWORDS: epitaxy, polarization, piezoresponse, double-exchange, Gilbert damping.

This abstract is approved as to form and content

_____

Kartik Ghosh, PhD
Chairperson, Advisory Committee
Missouri State University

STUDY OF MULTIFERROIC PROPERTIES OF FERROELECTRIC-FERROMAGNETIC HETEROSTRUCTURES BZT-BCT/LSMO

By

Md Abdullah-Al Mamun

A Masters Thesis
Submitted to the Graduate College
Of Missouri State University
In Partial Fulfillment of the Requirements
For the Degree of Master of Science, Materials Science

August 2017

Approved:

_____
Kartik Ghosh, PhD

_____
Mahua Biswas, PhD

_____
Keiichi Yoshimatsu, PhD

_____
Julie Masterson, PhD: Dean, Graduate College

ACKNOWLEDGEMENTS

I would like to express my gratitude to my advisor, Dr. Kartik Ghosh, for the supervision, encouragement, and advice throughout my master's years. He has cared every step of my progress in the thesis. I would also like to thank Dr. Robert Mayanovic for his cooperation performing different experiments.

I would like to thank the department of Physic, Astronomy, and Materials Science for providing excellent lab facilities to complete my experiments. I am also thankful to the graduate students of our department to assist me different ways. I want to acknowledge Air Force Research Laboratory (AFRL) at WPAFB, Dayton OH for their cooperation to do some experiments there through my adviser.

I am thankful to my beloved wife Mohsina Jannat who keeps patience in time of difficulties of my research. She encouraged me at tough situations. Finally, I would like to thank my parents for their constant support.

TABLE OF CONTENTS

LIST OF TABLES

LIST OF FIGURES

OVERVIEW

In the last couple of decades, researchers focused on multiferroic (MF) materials due to widespread applications of advanced technology[1]. The MF materials possess two or more of the 'ferroic' order parameters-ferroelasticity, ferroelectricity, and ferromagnetism[2]. Some other non-primary order parameters such as ferrotoroidicity[3], antiferromagnetism, ferrimagnetism etc. MF properties exhibit in a material mainly due to the presence of magneto-electric (ME) coupling. The ME coupling refers to the impact on the electric polarization through the change in magnetic field or the impact on magnetization through the change in electric field. The ME coupling is a unique feature that has a tremendous effect on technology with applications in solid-state transformers, multiple-state memories[4], data-storage media, high sensitivity magnetic field sensors, actuators, and spintronic[5]. The goal of the research is to find or develop materials which would possess both the ferroelectric and ferromagnetic properties in its single phase. But due to the basic difference in the mechanism of ferroelectricity and ferromagnetism, there exist very few materials in nature with the MF property[4].

The most recognized MF material is $BiFeO_3$ (BFO) which displays the co-existence of spontaneous electric and magnetic ordering in the same phase at room temperature[6]. But for commercial applications with BFO, some limitations must be overcome. It has a high leakage current and behaves like an antiferromagnetic material which weakens the magnetization at room temperature. So, the improvement of both the properties is mandatory for further applications. To enhance the MF properties some researcher doped rare earth (RE) and transition metal (TM) ions into BFO[7]. The RE ion

as a dopant degrades the ferroelectric polarization[8]. Therefore, researchers have been trying to figure out the MF properties of other materials also. Some other reported MF materials are $YMnO_3$[9], $BiMnO_3$[10], $TbMnO_3$[11], $DyMnO_3$[12], and some hexaferrite[13]. Also, there are several reports on MF properties of composite materials or heterostructures. Currently, researchers are working on the heterostructures of BFO/CoFe[14] and BFO/CoFeB[15]. However, a system has yet to be experimentally demonstrated which will be electrically and magnetically tunable. In my thesis, heterostructure of ferroelectric BZT-BCT and ferromagnetic lanthanum strontium manganese oxide (LSMO) has been used to investigate MF properties.

The precursor of BZT-BCT is $BaTiO_3$ (BTO) which is mainly used as a dielectric rather than a piezoelectric material because of its poor piezoelectric properties ($d33 \sim$ 200 pC/N) and low Curie temperature $T_c \sim 120^oC$[16]. But through doping with suitable donor or acceptor ions, the Curie temperature and electrical resistance of BTO can be altered[17]. Doping of zirconium (Zr) into titanium (Ti) site increases the chemical stability of the system and doping of calcium (Ca) into barium (Ba) site decreases the polymorphic phase transition (PPT) temperature significantly in BTO[18]. Therefore, $BaZr_xTi_{1-x}O_3$ (BZT) and $Ba_yCa_{1-y}TiO_3$ (BCT) have been extensively studied for the future non-toxic (Pb-free) ferroelectric/piezoelectric materials.

BZT-xBCT is a solid solution of rhombohedral (R3m) BZT and tetragonal (P4mm) BCT with an MPB (near x = 0.5). Recently, Liu and Ren reported that the bulk ceramics of a Pb-free BZT-xBCT system has a high piezoelectric coefficient ($d_{33} \sim 620$ pC/N) near the MPB[19]. Their reported piezoelectricity is comparable to that of Lead Zirconate Titanate (PZT) and even it is superior to that of existing Pb-free systems. The

improved dielectric, piezoelectric and ferroelectric properties are due to the MPB starting from a tetragonal-cubic-rhombohedral triple point which flattens the energy barrier for lattice distortion and polarization rotation from (001)T state to (111)R state[20]. Also, there might be an intermediate orthorhombic (Amm2) phase, separating the tetragonal and rhombohedral phases which eases the rotation of ferroelectric domains[21].

On the other hand, the ferromagnetic LSMO is a mixed-valence manganite which is an optimal source of fully spin-polarized carriers and shows a rich physics of magnetic phases and transport mechanisms[22]. When lanthanum ions (La^{3+}) in lanthanum manganese oxide, $LaMnO_3$ are partially substituted with divalent ion Sr^{2+}, a mixed valence state of Mn^{3+} and Mn^{4+} is generated, leading to a dramatic change in physical properties, such as insulating to metal transition, colossal magnetoresistance (CMR), and paramagnetic to ferromagnetic transition[23]. These characteristics can be tuned by changing Sr dopant concentration in LSMO which prompts applications in magnetic devices[24].

LSMO shows high-spin polarization due to its half-metallic nature arising from conducting electron. The high-spin feature makes LSMO reliable for applications in spin-dependent transport devices such as magnetic tunneling junction[25], spin-valves[26], read heads in hard disk drive, magnetic random access memory (MRAM), and data transfer in the magnetic recording system. The switching speed of those applications is limited due to the magnetic damping of the system. Also, the switching current behavior of the spin-torque transfer (STT) system[27] and the thermal magnetic noise of TMR read heads[28] depend on the damping constant. Different applications demand different values of damping constant. The damping constant for the STT based MRAM must be small to

minimize the power consumption. On the other hand, for the read sensors, a large damping constant is expected to improve the thermal stability[29]. Therefore, nowadays the researcher focused to understand the damping mechanism and control parameters to ensure the applications. In this respect, it is necessary to explore the magnetic dynamics and to tune the damping properties of LSMO for realizing high-speed spintronic devices.

A considerable number of substrates are commercially available which have comparable lattice parameters to manganite perovskite materials. They can be used as a template for the growth of LSMO thin films. Widely used substrates are $NdGaO_3$ (NGO), $(LaAlO_3)_{0.3}$-$(Sr_2AlTaO_6)_{0.7}$ (LSAT), $SrTiO_3$ (STO), $DyScO_3$ (DSO), and $LaAlO_3$ (LAO). The lattice parameters are respectively 3.85, 3.87, 3.905, 3.95, and 3.78Å. Among them, STO, and LSAT are cubic crystals, NGO, and DSO are orthorhombic crystals and LAO has the rhombohedral distorted perovskite crystal structure, which is a direct match with LSMO. We have used LAO for the growth of all the thin films as it shows low dielectric loss and it has minor lattice mismatch with LSMO. Moreover, to investigate the dynamic interface properties with a conducting material, we deposited LSMO thin film on platinum (Pt) substrate. The actual structure of the substrate is $Pt/Ti/SiO_2/Si$. The Pt coated silicon wafers have several advantages. The lattice constant of Pt is 4.0Å, which means a minimum lattice mismatch with LSMO. In addition, Pt layer is a polycrystalline layer and hence it helps during crystallization of thin films. It also improves the adhesion between the substrate and the thin film itself. The additional advantage of Pt is that it has oxidation resistance capability. The high oxidation temperature of Pt, compared to other metals as Gold and Silver, make it ideal for high temperature depositions as perovskite

phase stabilizes at high temperature only. The intermediate layer Titanium (Ti) is needed due to less adhesion of Pt to SiO_2.

Several factors influence the properties of the thin film such as growth temperature, background pressure, annealing media, annealing time, oxygen desorption rate, film thickness, energy density of the excitation source etc. Besides these parameters, a smooth surface morphology is necessary for the applications of LSMO and BZT-BCT. Properties of the thin film are very sensitive to the amount of oxygen present during the deposition. Too much oxygen yield three-dimensional growth while too little oxygen yields inferior ferromagnetic properties. Structural order plays a vital role to the stabilization of ferromagnetic and conductive behaviors of the film. Therefore, a tunable and controlled growth approach is a must. Focusing on ideal layer-by-layer growth can compromise the functional properties of the film. In this respect, among various deposition techniques, pulsed laser deposition reveals a well-suited choice.

In this thesis, thin film heterostructures of BZT-BCT(FE)/ LSMO(FM) on two different substrates-LAO and Pt have been investigated. The heterostructure on LAO substrate was used to analyze static properties whereas both the heterostructures were used for dynamic magnetic studies. Structural qualities have been investigated using XRD and Raman spectroscopy. The ferroelectric layer shows a high degree of polarization, a low leakage current, and a typical frequency dependent capacitance behavior. The ferromagnetic layer continues to show its ferromagnetism up to a high temperature (365K). MFs properties at microscale were investigated using piezoresponse force microscopy (PFM) and magnetic force microscopy (MFM). FMR spectroscopy has been used to study the dynamic magnetic properties.

FABRICATION AND CHARACTERIZATION OF FERROELECTRIC (FE)-FERROMAGNETIC (FM) HETEROSTRUCTURES BZT-BCT/LSMO/LAO USING PULSED LASER DEPOSITION

Abstract

Ferroelectricity and ferromagnetism have been investigated in lead (Pb)-free $0.5Ba(Zr_{0.2}Ti_{0.8})O_3$-$0.5(Ba_{0.7}Ca_{0.3})TiO_3$ (BZT-BCT)/$La_{0.7}Sr_{0.3}MnO_3$(LSMO) heterostructures for multiferroic applications. BZT-BCT thin films were grown on LSMO/ lanthanum aluminate (LAO) by pulsed laser deposition (PLD) technique. Prior to that, LSMO was deposited on single-crystal LAO substrate by PLD. The epitaxial growth of the highly-oriented (00l) films was confirmed by XRD pattern. The small FWHM (0.11^o) of the rocking curve peak performed about (00l) peak indicates the better out-of-plane orientation of the film. The polarization switching behavior has been observed with a remnant polarization of 93.3 $\mu C/cm^2$ and a coercive field of 159.89 kV/cm saturates at 5V applied voltage. The low value (0.02) of the dielectric loss confirms the high quality of the ferroelectric thin film. A well-behaved room temperature *M-H* curve has been observed for LSMO/LAO through superconducting quantum interference device (SQUID) magnetometer indicating the ferromagnetic behavior of the film. The temperature-dependent magnetization of the film shows paramagnetic to ferromagnetic transition at about 365K, which is comparable to the bulk samples and recently reported value as well. These results guide researchers to develop next-generation heterostructures using BZT-BCT and LSMO for multiferroic applications.

Introduction

MF materials simultaneously exhibit ferroelectricity and ferromagnetism in its single phase[1]. They can provide the desired ME coupling between the two order parameters which enable applications in magnetic data storage[2], solid-state transformers, spintronic devices, high sensitivity magnetic field sensors, and actuators[3]. The researcher devoted themselves to combine electrical and magnetic properties in one single material which yielded new MF materials[4]. Up to today, the most reported MF material is $BiFeO_3$[2]. Also some other materials such as $YMnO_3$[5]. $TbMnO_3$[6], $DyMnO_3$[7], and hexaferrites[8] attracted much to the researcher. However, researchers reported some drawbacks such as high leakage current, weak magnetism at room temperature etc. that limits the MF applications using those materials. To enhance the MF properties some researcher doped rare earth (RE) and transition metal (TM) ions into BFO[9] but the RE ion as a dopant degrades the ferroelectric polarization[10]. In addition, there are several reports on MF properties of composite materials or heterostructures. Currently, researchers are working on the heterostructures of BFO/CoFe[11] and BFO/CoFeB[12]. However, a system has yet to be experimentally demonstrated which will be electrically and magnetically tunable. In this study, I used heterostructure of ferroelectric BZT-BCT and ferromagnetic LSMO to investigate MF properties. There is no report of heterostructure composed of that two materials. For MF applications, the study of the properties of such heterostructure is vital. In this study, the ferroelectric BZT-BCT shows a high degree of polarization with low leakage current while the ferromagnetic LSMO continues to show its ferromagnetism up to a high temperature. The shift in the hysteresis loop for the heterostructure indicated the possible magnetoelectric coupling between the ferroelectric

and ferromagnetic layers. Details of the structural property correlation of BZT-BCT/LSMO/ LAO will subsequently be discussed in the result and discussion section.

Experimental

Ferroelectric BZT-BCT ceramic target was prepared by a standard solid state reaction using high purity chemicals $BaCO_3$ (99.9%, Inframat Advanced Materials), CaO (99.95%, Alfa Aesar), TiO_2 (99.9%, Sigma-Aldrich), and ZrO_2(99.9%, Inframat Advanced Materials) in appropriate proportions. Polyvinyl alcohol (PVA) was added to the mixture to prevent agglomeration of the powder particles. The final mixer was pressed with a 'hydraulic press' to form the target. After that, the prepared target was calcined at 1350 C and then sintered at 1450 C in air. On the other hand, a high purity dense LSMO target was purchased from Kurt J. Lesker Company. The target was 99.9% pure, 1.00" diameter×0.250" thick, +/-0.010" AL. A CMP polished highly oriented (001) LAO substrate (2" dia +/- 0.5 mm × 0.5 thickness +/-0.05 mm) was purchased from MTI Corporation. The configuration of the substrate was as follows: surface finish (RMS or Ra): < 8A with free sub-surface damaged, under 1000 class clean room, and in 100 grade plastic bag in a wafer container.

Thin films of LSMO and then BZT-BCT were deposited on LAO substrates by Pulsed Laser Deposition (Excel Instrument, PLD-STD-18) technique. A KrF excimer laser (Lambda Physik, COMPEX 201) with an energy density of 2 Jcm^{-2}, the wavelength of 248 nm, pulsed duration of 20 ns, was used with 10 Hz pulse rate for the deposition. Thin films were grown at different growth temperatures (600^0C to 850^0C) and different oxygen pressures (10^{-1} to 10^{-4} mbar). The best performance was observed in the film

grown at the growth temperature of 800ºC with 4.1×10^{-1} mbar oxygen pressure. The base pressure of the chamber was below 1×10^{-5} mbar. After the desired number of PLD shot, the deposited film was cooled down to room temperature maintaining the oxygen pressure at 110 mbar. The average film thickness was 100 nm, measured ex-situ by a profilometer (Veeco, Dektak 150).

Thin films were characterized by X-ray Diffractometer (Bruker, D8 Discover) using θ-2θ scan in the range of 20° to 80° maintaining the Bragg−Brentano reflection geometry. The excitation source was an x-ray with the wavelength of 1.5405Å. The vibrational properties of the samples were characterized by micro-Raman scattering experiments (Horiba Labram Raman-PL System) with a 532 nm green laser excitation source. The experiments were performed in a back-scattering geometry with 15 seconds exposure time, and 20 accumulation cycles. The measured spot size was approximately 2.5 μm in diameter on the thin film. We were aware of the possible damage of the thin film due to the excitation source. The Raman spectroscopy was collected through NGS Labspec-5 software in the range of 100 cm^{-1} to 1000 cm^{-1}. The data were analyzed by Gaussian-Lorentzian peak fitting using Origin Pro 8.5.1.

Temperature and magnetic field dependent magnetization of the films were measured by a SQUID magnetometer (Quantum Design, MPMS 5XL) interfaced through MultiVu software. The temperature was varied from 5k to 370k. The M-H hysteresis loop of the sample was observed by varying magnetic field from -5000 Oe to +5000 Oe. The maximum sensitivity of the magnetometer was 10^{-9} emu. Polarization measurement was carried out by Sawyer-Tower technique. Au-Ti top electrodes were deposited onto the thin film by thermal evaporation using a physical mask on the thin film. The diameter of

the electrodes was 100 to 200μm. The data were analyzed through Origin Pro 8.5.1 software.

Results and Discussion

Figure 1 presents XRD plots of BZT-BCT/LSMO (black) and only LSMO (red) thin films on LAO substrate. It can be observed that both the samples exhibit a complete single-phase perovskite structure. There is no evidence of secondary phases such as $Ba_3Ca_2Ti_2O_9$ and the possibility of such impurity is minimized by sintering at higher temperatures[13]. Due to the complete solid solubility of Ca^{2+} at Ba-site and Zr^{4+} at Ti-site at the higher sintering temperature, no other secondary phase was observed in the present BZT–BCT ceramics.

It should be noted that the highly-oriented thin films demonstrated a weak splitting, which could be induced by formation of multiple domains, e.g., a- and c-domains, analogous to the case of PZT[14]. The splitting of XRD peak in the 2θ range of 43.5 to 44.5 is a unique characteristic of the tetragonal phase in BZT-BCT. The single (002) plane corresponding to cubic phase transforms into (200) and (002) crystallographic planes, which are the characteristics of a tetragonal structure[15]. The inset XRD plot in Figure 1 corroborates the presence of tetragonal crystallographic structural symmetry in the PLD grown thin film. The asymmetricity of the peak shape indicates the existence of tetragonal and cubic phases. This tetragonal structure might partly be a consequence of averaging $\langle 111 \rangle$ displacements of octahedral Ti^{4+} (local rhombohedral structure)[16]. The splitting of peaks must not be attributed to the presence of CuK_{α} or CuK_{β} at higher

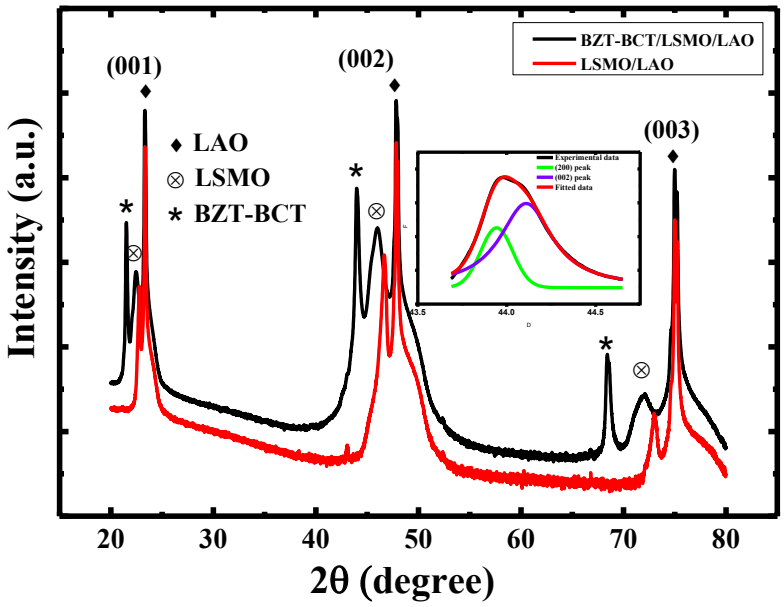

Figure 1. X-ray diffraction pattern of both LSMO (red line) and BZT-BCT/LSMO (black line) on LAO substrate. The inset plot shows the splitting of (002) peak, which is a characteristic of the tetragonal crystal structure.

angles, as this is predominantly seen in the mentioned 2θ range (43.5 to 44.5). In addition, the (003) diffraction peak at 68.5º shows mixed diffraction peaks, which is consistent with Liu's results[17]. Such coexistence plays a key role in enhancing the piezoelectric performance. To further investigate the texture of the films, we performed XRD rocking curve around BZT-BCT (002), BZT-BCT (003), and LSMO (002) plane, which are displayed in Figure 2(a), 2(b), and 2(c) respectively. The FWHM (θ) of the rocking curves are 0.10°, 0.14°, and 0.37° respectively. The small values of FWHM confirmed the oriented nature of the films.

The *c*-axis lattice constants of LSMO calculated from the XRD data for LSMO/ LO and BZT-BCT/LSMO/LAO are 3.892 and 3.943 Å, respectively. As the lattice

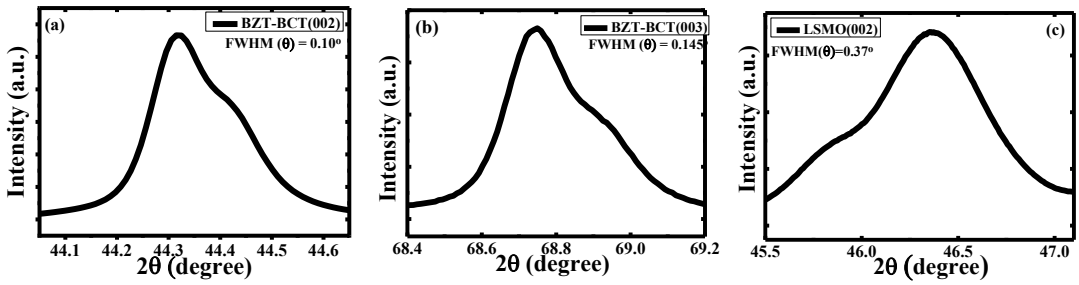

Figure 2. High resolution rocking curve profiles for the (a) BZT-BCT (002) (b) BZT-BCT (003), and (c) LSMO (002) reflections. Horizontal axes are shown in the relative angles of 2θ in degree. Vertical axes are shown in the arbitrary units. The FWHM (θ) of the reflections are 0.10°, 0.145°, and 0.37°, respectively.

constant of bulk LSMO is 3.889 Å, this induces tensile strain in the LSMO thin film. However, the scenario is critical for the heterostructure. The BZT-BCT/LSMO/ LAO heterostructure experiences two strain effects, one incurred from the strain of LSMO/ LAO due to the lattice mismatch between the film and the substrate and the other from the BZT-BCT/LSMO interface. Table 1 shows the experimental and standard values of the c-axis lattice parameters.

In addition to XRD analysis, we performed room-temperature Raman experiment to investigate the molecular vibrational modes present in the crystal lattice. Raman spectroscopy is a highly responsive technique to evaluate the atomic structure and phases of the materials. The cubic perovskite structure inherently has no Raman active modes while the tetragonal structure shows some significant modes[18]. The phases of ABO_3 type

Table 1. Experimental out-of-plane lattice parameters from XRD (all the values in Angstrom)

	BZT-BCT	LSMO	LAO
LSMO/LAO		3.892	3.802
BZT-BCT/LSMO /LAO	4.117	3.943	3.802

perovskite crystals are interesting. For example, tetragonal $BaTiO_3$ has five atoms and there are fifteen degrees of freedom present per unit cell[19]. It behaves as a ferroelectric crystal below its transition temperature (T_t ~120°C) and the vibrational modes are Raman active up to T_t. The cubic phase above T_t is essentially Raman inactive and can be easily distinguishable from the Raman active tetragonal structure[20]. The Raman spectrum of tetragonal BZT-BCT thin film shown in Figure 3 exhibits the following six active modes: 2 A_1(TO), 1 A_1(LO), 1 E(TO), 1 E(LO), and 1 B_1. Each of the A_1 and E modes split into TO (transverse optical) and LO (longitudinal optical) modes due to the presence of long-range electrostatic forces[21].

The signature Raman peaks in the BZT-BCT thin film are observed at 179.94, 320.51, 543.35, and 748.31 cm^{-1}. The peak at 179.94 cm^{-1} corresponds to the A_1 (TO) mode of vibration[22] which represents the Ti-O phonon vibrations of BZT-BCT. Another A_1 (TO) mode at around 543.35 cm^{-1} represents the O-Ti-O symmetric stretching

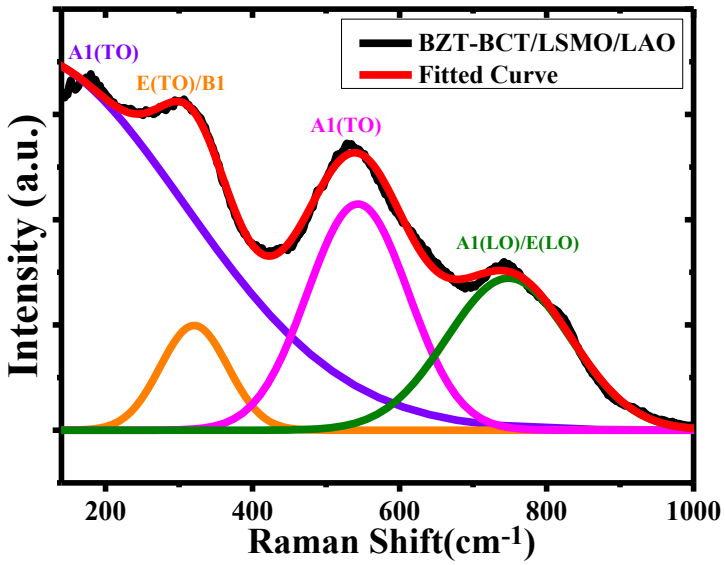

Figure 3. Raman spectra of BZT-BCT/LSMO thin film on LAO substrate with Gaussian and Lorentzian peak fitting by using Origin software.

vibrations[23]. These vibrations are caused due to the presence of non-centrosymmetric regions in which a Ti or Zr atom is displaced from its octahedral position because first-order Pm3m Raman scattering is symmetry-forbidden in the centrosymmetric space group[24]. The sharp feature at 543.35 cm^{-1} indicates the high quality of the thin film. The peak at 320.51 cm^{-1}, attributed to the B_1 mode, is a characteristic peak for BZT–BCT and indicates the asymmetry of the TiO_6 octahedra[25]. This band is considered to be the Raman signature of the tetragonal phase. The interesting feature in the Raman spectra of our BZT-BCT thin film is the absence of the A_{1g} octahedral breathing mode at 800 cm^{-1} which was observed in their bulk counterparts[26]. The breathing mode is associated with more dissimilar ions on B-site of the Raman active perovskite[27]. The absence of breathing mode demonstrates that Ca^{2+} resides on the Ba-site, not on the Ti-site in our case.

The broadening and peak shift of A_1 (LO) vibrational mode at 748.31 cm^{-1}, compared to its bulk counterpart, is a characteristic feature of the tetragonal phase. The broadening represents the distortion in the thin film. Both the peak position and the broadening of this mode are related to the non-centrosymmetric region in the unit cell. The weak intensity of some of the vibration bands of the BZT–BCT film denotes the heavily damped phonons. The A_1 (TO) mode at 543.35 cm^{-1} and A_1 (LO) mode at 748.31 cm^{-1} have a vital contribution in the polarization kinetics. The displacement of Ti/Zr ions from its octahedral position causes an increase in the dipole moment of the unit cell which finally increases the polarization.The peak positions of some of the modes such as B_1/E (TO) and A_1 (LO) / E (LO), shift towards either the lower or higher frequency region. This phenomenon of upshift/downshift in Raman spectrum indicates the localized chemical environments and/or strain[19]. As the BZT-BCT thin films were deposited under

the same PLD conditions, the deviation of chemical composition can be ruled out which has also been confirmed by XRD analysis. So, the epitaxial strain originating from both the substrate and the LSMO layer responsible for the shifting of Raman modes. Yamada *et al*. explained the strain relaxation process by surface energy variation in the different crystallographic surface in Barium Strontium Titanate (BST) system[28]. The LSMO thin film in our study yields a much lower vibrational frequency to be detected in the Raman spectroscopy due to its half-metallic nature.

The well-defined peaks in the Raman spectroscopy prove the high quality of the thin film. Taken together, the XRD and Raman spectroscopy results indicate the presence of non-centrosymmetric regions that result from the local off-centering of the titanium (zirconium) atoms. Table 2 represents the peak positions and full width at half maximum (FWHM) of the corresponding vibrational modes in the BZT-BCT thin film.

The polarization (P) vs electric field (E) hysteresis loop is the proof of the ferroelectricity in a material. Figure 4 shows the experimental P-E curves of an Au-Ti/BZT-BCT/LSMO ferroelectric capacitor. The curves are nothing but a hysteresis loop which is the indication of the ferroelectricity in the thin film. The hysteresis loops are almost centered along the y-axis. As the voltage increases, the capacitor starts to show hysteric characteristics and saturates at a higher voltage. Table 3 shows the remnant polarization, saturation polarization along with the applied voltage and coercive field for the sample Au-Ti/ BZT-BCT/LSMO ferroelectric capacitor. The experimental values are mentioned with their units.

Table 2. Peak positions and FWHM of the corresponding vibrational modes observed in Raman spectroscopy

Peak Position (cm^{-1})	Vibration mode	FWHM (cm^{-1})	Reason
179.94	A_1(TO)	518.25	Ti-O phonon vibration
320.51	E(TO)/B_1	108.61	Raman signature
543.35	A_1(TO)	162.36	O-Ti-O symmetric stretching vibrations;
748.31	A_1(LO)/E(LO)	198.21	Raman signature

The P-E hysteresis loops yield a large remnant and saturation polarization in our BZT-BCT thin film. It showed a maximum remnant polarization (P_r) of 93.3 μC/cm^2 and a coercive field (E_c) of 159.89 kV/cm for the MPB composition at 5V applied voltage. The reason behind the high remnant polarization in the PLD grown thin film is the

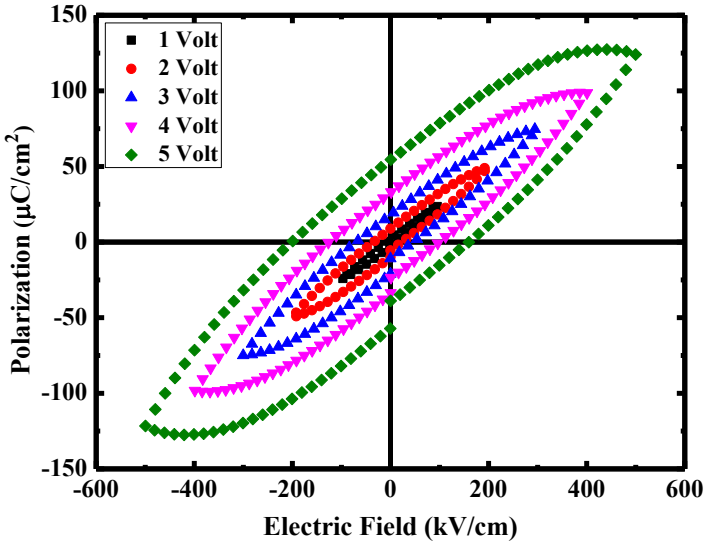

Figure 4. Polarization-electric field (P-E) hysteresis loops for ferroelectric capacitors Au-Ti/BZT-BCT/LSMO at different applied voltages

Table 3. Remnant and saturation polarization with coercive field at different voltages applied to FECAP

Applied Voltage (volt)	Remnant Polarization, P_r ($\mu C/cm^2$)	Saturation Polarization, P_s ($\mu C/cm^2$)	Coercive Field, E_c (kV/cm)
1	4.36	26.2	5.87
2	14.3	55.1	23.31
3	28.8	85.8	46.13
4	56.3	122	99.14
5	93.3	163	159.89

uniform distribution of grain sizes, compositional homogeneity, absence of domain-wall pinning centers, and low defect density as described previously[29].

The observed coercive field was also higher than that of the BZT-BCT bulk ceramic (1.68 kV/cm)[30]. The much higher coercive field is a consequence of much smaller grains and substrate clamping effect[31]. As the average grain size is small in PLD grown thin films compared to their bulk counterpart, the length of the grain boundaries per unit volume is higher. This requires higher electric field to orient all the domains along the field direction. The orientation-dependent analysis by Luo *et al*. demonstrated that (001) oriented thin film shows superior ferroelectricity rather than (110) and (111)-oriented thin film[30]. In this work, our sample is highly oriented along (001) direction, which upholds the high polarization phenomena in the BZT-BCT samples.

The dielectric properties of the BZT–BCT thin film were measured at room temperature as a function of frequency ranging from 1 kHz to 50 kHz with an exciting voltage of 1 V. Both the electrodes were thermally evaporated Au-Ti. The top electrode

was on the ferroelectric layer whereas the bottom electrode was taken from the half metallic LSMO layer. Figure 5(a) and 5(b) represent the typical frequency dependent dielectric constant and dielectric loss in a wide range of frequencies respectively. With increasing frequency, dielectric constant decreases but the loss tangent increases. The measured largest capacitance is 2.79 nF which yields a high dielectric constant of 5100 because the spontaneous polarization vector points are normal to the (001)-oriented film surface and coincide with the dielectric measuring direction[32].

The leakage current and the time-dependent dielectric break-down (TDDB) are vital issues for applications in electronics and memory devices. For a capacitor, which should completely block direct current (dc), the leakage current is the amount of dc current that flows at some dc bias. In a different way, we can say that the leakage phenomenon is a gradual loss of energy from a charged capacitor. The electronic devices have different regions of operation, such as active region, saturation region, cut-off region etc. The leakage current is the small amount of current that flows through the device even the

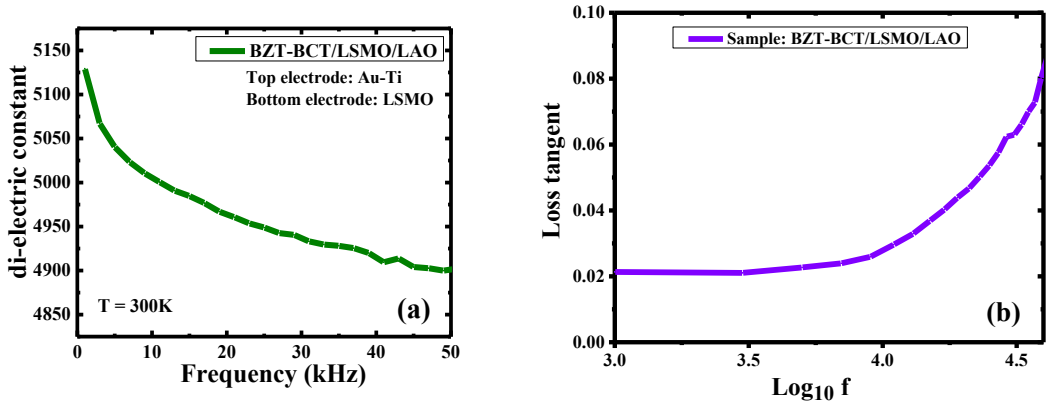

Figure 5. Frequency dependence of dielectric constant (a) and dielectric loss (b) for BZT–BCT/LSMO thin film on LAO substrate. A wide range of frequencies was applied from 1KHz to 50KHz. The dielectric loss was plotted against logarithm of the frequency.

device is ‘turned off’. Though, this current is really small compared to ‘on current’, it still slowly discharges the capacitor. In leakage analysis, the time to breakdown (t_{BD}) is another important characteristic of the device. This time is generally measured by applying a variable voltage until dielectric breakdown. It is usually assumed that t_{BD} is a function of the total number of charged carriers passing through the films. Therefore, t_{BD} is inversely proportional to the leakage current density (J)[33].

Most of the literature have demonstrated the ferroelectric properties and leakage behavior of BZT-BCT deposited on the metal electrode (for example Pt)[34]. Hwang *et al*. reported that, in general, thin films on metal electrodes exhibit lower leakage current density and withstand higher dc voltage without a dielectric breakdown in comparison to oxide electrodes[35]. Our ferroelectric material was deposited on oxide material (LSMO) and we have used that as the bottom electrode. So, it is a must to determine the leakage behavior of BZT-BCT with LSMO as an electrode.

Figure 6 depicts the typical room temperature leakage current density-time (J-t) profiles assessed at two different applied electric fields of 100 kV/cm and 400 kV/cm for the BZT-BCT thin film. Both the current densities show similar behavior with respect to time passes. Initially, the leakage currents increase gradually with time and after a while reached a saturated steady state. The leakage current at low electric field reaches steady state faster than that at the higher electric field. The steady state values of the leakage currents at low and high fields are 15.9 and 78.1 $\mu A/cm^2$ respectively which are very much comparable with reports on ferroelectric material with a metal electrode[36]. The ferroelectric material is ideally expected to possess very high electrical resistance. However, several factors such as cationic/anionic vacancies, structural distortions, grain

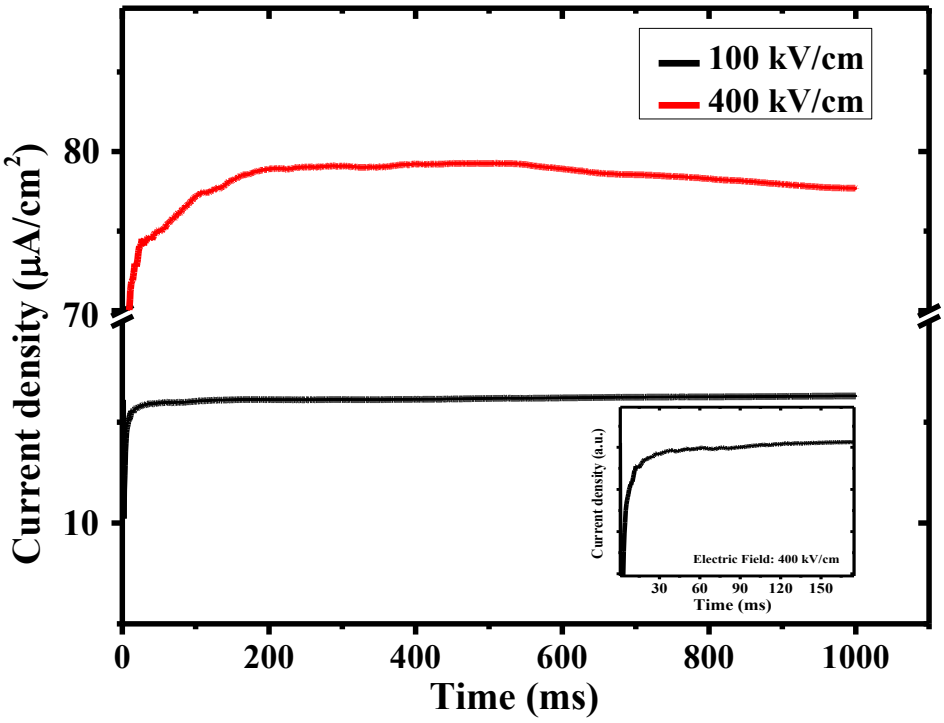

Figure 6. Leakage current characteristics of Au-Ti/BZT-BCT/LSMO with two different applied electric fields 100 kV/cm (black line) and 400 kV/cm (red line).

boundaries, film-electrode interface, etc., act as low resistance channels, thereby contributing to the mobility of charges in terms of leakage current. In our sample, as the leakage currents are very small, a higher time to breakdown is expected of our heterostructure.

PLD grown LSMO thin film was highly epitaxial stimulated by monocrystalline LAO substrate at higher deposition temperature. Figure 7(a) shows the M-H curve of LSMO/LAO thin films with the field applied parallel to the film plane at room temperature. Figure 7(b) shows the low field fragments of the hysteresis loops. The magnetization was calculated after subtraction of a diamagnetic background from the substrate. The magnetization increases with increasing magnetic field until saturation is

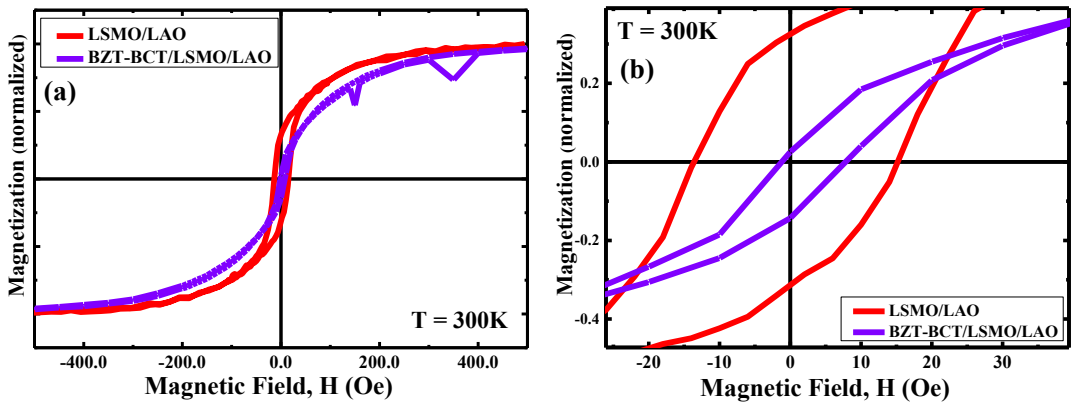

Figure 7. (a) Magnetization-Applied field (M-H) hysteresis loop of LSMO/LAO (red), BZT-BCT/LSMO/LAO (purple) obtained at room temperature and (b) the low field fragments of the hysteresis loops of figure (a)

reached at 500 Oe. A well-behaved M-H curve was observed for the LSMO thin film which is the indication of ferromagnetism in the sample. It is worth noting that the magnetic disorder at the surface has been suggested to be considerably larger than in the bulk. In perovskite material, the cubic symmetry lacks at surfaces and charge is transferred from the bulk to the surface layers, leading to the formation of $Mn3+$[37].

Figure 8 shows the temperature dependence of magnetization (M-T curve) of the LSMO/LAO sample at two different magnetic fields (High field of 5000 Oe and Low field of 100 Oe). The measurements were performed in a field-cooled condition, known as FC magnetization. Both the M-T curves reveal the Curie temperature (T_c) of the sample. The commencement of a spontaneous magnetization near T = 365K indicates T_c of the ferromagnetic thin film. Table 4 summarizes values from SQUID measurement.

The surface morphology (topography) of the LSMO thin film deposited on LAO substrate is shown in Figure 9(a). There are no distinctive domain structures and domain walls found in the topography. However, the color contrast reveals the existence of

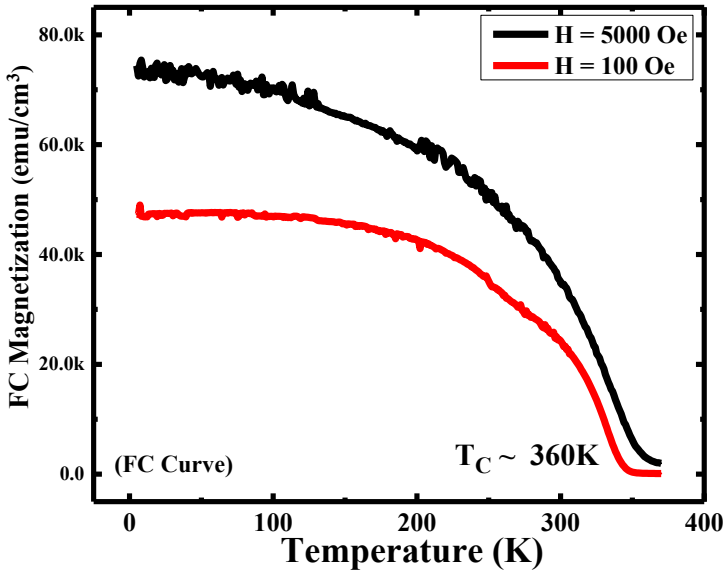

Figure 8. Temperature dependence of magnetization for LSMO/LAO at different applied magnetic fields.

different domains in the sample. The MFM phase image is shown in Figure 9(b). The image contrast of the phase image is a clear indication of the magnetic activity present in the sample. The contrast shown by the MFM image occurs because of force gradients between the FM tip and the magnetic activity present on the sample's surface. The phase image was achieved after topography measurements (tapping mode) followed by sample surface scanning at a constant height (lift mode). According to this procedure, no van der

Table 4. Results from SQUID measurement

Results from M-H hysteresis loop		Results from M-T curve	
Saturation Magnetization,	32 kemu/cm^3	Field	Curie Temperature
Remnant Magnetization, M_r	11 kemu/cm^3	H = 5000 Oe	T_C = 365.2 k
Coercive field, H_c	15.19 Oe	H = 100 Oe	T_C = 354.18 k

Waals forces are expected to be detected, and any change in the vibration amplitude of the cantilever is proportional to the gradient of magnetic fields perpendicular to the sample surface.

The surface morphology of BZT-BCT film is shown in Figure 9(c). There is no evidence of cracking or defects on the surface. Furthermore, the topography is very much uniform which is an indication of a homogenous PLD deposition. From PFM surface morphology observation, it can be inferred that the BZT–BCT film exhibits a uniform and dense microstructure. Moreover, based on the substrate orientation dependence of the equilibrium grain shapes of the BZT-BCT thin film and the Winterbottom construction theory, it could be visualized that our BZT-BCT thin film maintains a layer-by-layer growth along the lowest energy surface for (001)-orientation[38]. The PFM phase image for the BZT-BCT thin film was obtained utilizing commercially available conducting tip in contact mode by applying a DC voltage of 1 volt between the tip (top electrode) and the bottom electrode (LSMO) grounded. The out-of-plane PFM phase image is shown in Figure 9(d). The phase image distinguishes the domains of opposite polarization with dark and bright contrast in the image. After scanning with a signal to the tip with respect to sample surface, a piezoelectric contrast (shown by the bright and dark shades) appears, result in spontaneous polarization, which can be switched by applying an external excitation. Therefore, we can conclude that the ferroelectricity in the BZT–BCT film at the nanoscale level can be confirmed using PFM.

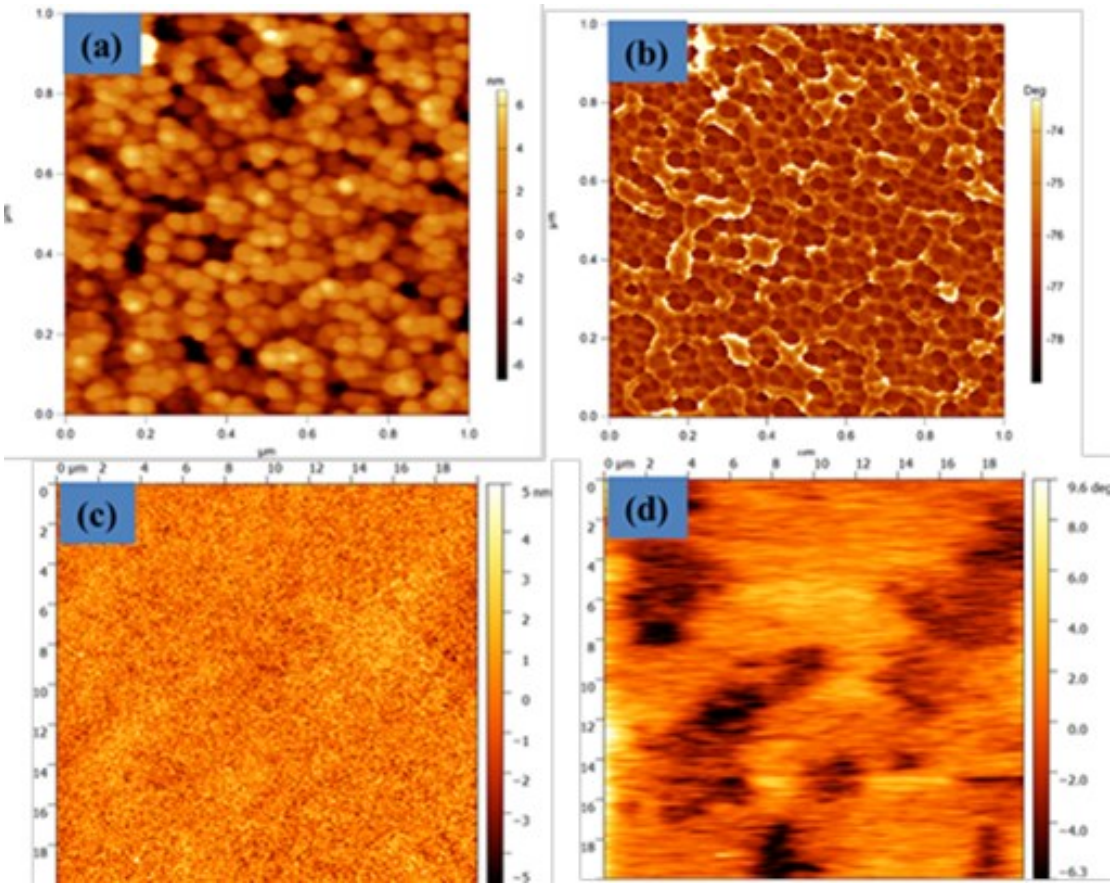

Figure 9. (a) Surface topography of LSMO (b) MFM phage image of ferromagnetic LSMO thin film on LAO substrate and (c) surface topography of BZT-BCT film and (d) PFM phage image of ferroelectric BZT-BCT thin film on LAO substrate.

Conclusions

Highly oriented ferroelectric-ferromagnetic heterostructure was fabricated using PLD. Along with the theta-2theta scan of XRD, the small full width at half maximum (FWHM) at high-resolution XRD rocking curve corroborates the oriented nature of the films. The BZT-BCT ferroelectric thin film shows polarization switching behavior with a large remnant polarization of 93.3 $\mu C/cm^2$, a high coercive field of 159.89 kV/cm, and a large dielectric constant with negligible loss. The well-behaved M-H hysteresis loop at room temperature confirms the ferromagnetic nature of the LSMO thin film with high

saturation and remnant magnetization. Temperature dependent magnetization data confirm a high Curie temperature of 360k, which is very close to the bulk sample. Further, PFM and MFM of the ferroelectric and ferromagnetic thin film, respectively reveal the corresponding domain of the as-grown film. These results may guide researchers to develop next-generation Pb-free ferroelectric-ferromagnetic heterostructures using BZT-BCT and LSMO for applications with electro-mechanical, and magneto-electric coupling.

Acknowledgement

I would like to acknowledge Dr. Gail J Brown, Air Force Research Laboratory (AFRL), Wright-Patterson AFB, OH 45433, USA for providing support to collect the polarization data.

References

1. Cheong, S.-W. & Mostovoy, M. Multiferroics: a magnetic twist for ferroelectricity. *Nat Mater* **6,** 13–20 (2007).

2. Lottermoser, T. *et al.* Magnetic phase control by an electric field. *Nature* **430,** 541–544 (2004).

3. Vaz, C. A. F., Hoffman, J., Ahn, C. H. & Ramesh, R. Magnetoelectric coupling effects in multiferroic complex oxide composite structures. *Adv. Mater.* **22,** 2900–2918 (2010).

4. Lee, J. H. *et al.* A strong ferroelectric ferromagnet created by means of spin-lattice coupling. *Nature* **466,** 954–958 (2010).

5. Zaghrioui, M., Grenèche, J. M., Autret-Lambert, C. & Gervais, M. Effect of Fe substitution on multiferroic hexagonal YMnO3. *J. Magn. Magn. Mater.* **323,** 509–514 (2011).

6. Kimura, T. *et al.* Magnetic control of ferroelectric polarization. *Nature* **426,** 55–58 (2003).

7. Goto, T., Kimura, T., Lawes, G., Ramirez, A. P. & Tokura, Y. Ferroelectricity and Giant Magnetocapacitance in Perovskite Rare-Earth Manganites. *Phys. Rev. Lett.* **92,** 257201 (2004).

8. Kimura, T. Magnetoelectric Hexaferrites. *Annu. Rev. Condens. Matter Phys.* **3,** 93–110 (2012).

9. Films, B. T. & Kim, J. W. Effects of Transition Metal Ion Doping on Structure and Electrical Properties of. (2012). doi:10.1111/j.1551-2916.2012.05081.x

10. Zhang, S. *et al.* Observation of room temperature saturated ferroelectric polarization in Dy substituted BiFeO 3 ceramics. *J. Appl. Phys.* **111,** (2012).

11. Chu, Y.-H. *et al.* Electric-field control of local ferromagnetism using a magnetoelectric multiferroic. *Nat Mater* **7,** 478–482 (2008).

12. Béa, H. *et al.* Mechanisms of Exchange Bias with Multiferroic ${\mathrm{BiFeO}}_{3}$ Epitaxial Thin Films. *Phys. Rev. Lett.* **100,** 17204 (2008).

13. Puli, V. S. *et al.* Structure, dielectric, ferroelectric, and energy density properties of (1 - x)BZT-xBCT ceramic capacitors for energy storage applications. *J. Mater. Sci.* 1–7 (2012). doi:10.1007/s10853-012-6990-1

14. Yokoyama, S. *et al.* Dependence of electrical properties of epitaxial Pb(Zr,Ti)O 3 thick films on crystal orientation and Zr/(Zr+Ti) ratio. *J. Appl. Phys.* **98,** (2005).

15. Kolekar, Y. D., Bhaumik, a., Shaikh, P. a., Ramana, C. V. & Ghosh, K. Polarization switching characteristics of 0.5BaTi0.8Zr0.2O3-0.5Ba0.7Ca0.3TiO3 lead free ferroelectric thin films by pulsed laser deposition. *J. Appl. Phys.* **115,** 154102 (2014).

16. Page, K., Proffen, T., Niederberger, M. & Seshadri, R. Probing local dipoles and ligand structure in BaTiO3 nanoparticles. *Chem. Mater.* **22,** 4386–4391 (2010).

17. Tian, Y., Wei, L., Chao, X., Liu, Z. & Yang, Z. Phase Transition Behavior and Large Piezoelectricity Near the Morphotropic Phase Boundary of Lead-Free (Ba 0.85 Ca 0.15)(Zr 0.1 Ti 0.9)O 3 Ceramics. *J. Am. Ceram. Soc.* **96,** 496–502 (2013).

18. Wang, Z.-M. *et al.* Crystallization, phase evolution and ferroelectric properties of sol-gel-synthesized Ba(Ti0.8Zr0.2)O3-x(Ba 0.7Ca0.3)TiO3 thin films. *J. Mater. Chem. C* **1,** (2013).

19. Puli, V. S. *et al.* Barium zirconate-titanate/barium calcium-titanate ceramics via sol–gel process: novel high-energy-density capacitors. *J. Phys. D. Appl. Phys.* **44,** 395403 (2011).

20. Liu, W. & Ren, X. Large Piezoelectric Effect in Pb-Free Ceramics. *Phys. Rev. Lett.* **103,** 257602 (2009).

21. Kumar, A., Rivera, I. & Katiyar, R. S. Investigation of local structure of lead-free relaxor Ba(Ti0.70Sn0.30)O3 by Raman spectroscopy. *J. Raman Spectrosc.* **40,** 459–462 (2009).

22. Tang, X. G., Chew, K.-H. & Chan, H. L. W. Diffuse phase transition and dielectric tunability of Ba(ZryTi1−y)O3 relaxor ferroelectric ceramics. *Acta Mater.* **52,** 5177–5183 (2004).

23. Sczancoski, J. C. *et al.* Structure and optical properties of [Ba1–xY2x/3](Zr0.25Ti0.75)O3 powders. *Solid State Sci.* **12,** 1160–1167 (2010).

24. Scalabrin, A., Chaves, A. S., Shim, D. S. & Porto, S. P. S. Temperature dependence of the A1 and E optical phonons in BaTiO3. *Phys. Status Solidi* **79,** 731–742 (1977).

25. Moreira, M. L. *et al.* Hydrothermal Microwave: A New Route to Obtain Photoluminescent Crystalline BaTiO3 Nanoparticles. *Chem. Mater.* **20,** 5381–5387 (2008).

26. Reddy, Y. K. V., Mergel, D., Reuter, S., Buck, V. & Sulkowski, M. Structural and optical properties of BaTiO 3 thin films prepared by radio-frequency magnetron sputtering at various substrate temperatures. *J. Phys. D. Appl. Phys.* **39,** 1161–1168 (2006).

27. Use of Raman spectroscopy to determine the site occupancy of dopants in BaTiO3. *J. Appl. Phys.* **109,** 114110 (2011).

28. Yamada, T., Kamo, T., Su, D., Iijima, T. & Funakubo, H. Influence of Epitaxial Growth Orientation on Residual Strain and Dielectric Properties of (Ba0.3Sr0.7)TiO3 Films Grown on In-Plane Compressive Substrates. *Ferroelectrics* **405,** 262–267 (2010).

29. Zhang, S., Xia, R. & Shrout, T. R. Modified (K0.5 Na0.5) Nb O3 based lead-free piezoelectrics with broad temperature usage range. *Appl. Phys. Lett.* **91,** 0–3 (2007).

30. Luo, B. C., Wang, D. Y., Duan, M. M. & Li, S. 'Orientation-dependent piezoelectric properties in lead-free epitaxial 0.5BaZr0.2Ti0.8O3-0.5Ba0.7Ca0.3TiO3 thin films'. *Appl. Phys. Lett.* **103,** 122903 (2013).

31. Kang, G., Yao, K. & Wang, J. (1 − x)Ba(Zr0.2Ti0.8)O3-x(Ba0.7Ca0.3)TiO3 Ferroelectric Thin Films Prepared from Chemical Solutions. *J. Am. Ceram. Soc.* **95,** 986–991 (2011).

32. Li, W. L. *et al.* Giant piezoelectric properties of BZT–0.5BCT thin films induced by nanodomain structure. *RSC Adv.* **4,** 56933–56937 (2014).

33. Chen, J., Chen, H. & Lee, J. Y. An investigation on the leakage current and time dependent dielectric breakdown of ferroelectric lead–zirconate–titanate thin film capacitors for memory device applications. *Appl. Phys. Lett.* **69,** 4011–4013 (1996).

34. Das, R. R., Bhattacharya, P., Katiyar, R. S. & Bhalla, A. S. Leakage current behavior of SrBi2Ta2O9 ferroelectric thin films on different bottom electrodes. *J. Appl. Phys.* **92,** 6160–6164 (2002).

35. Hwang, C. S. *et al.* A comparative study on the electrical conduction mechanisms of (Ba0.5Sr0.5)TiO3 thin films on Pt and IrO2 electrodes. *J. Appl. Phys.* **83,** 3703–3713 (1998).

36. Chi, Q. G. *et al.* Interface optimization and electrical properties of 0.5Ba(Zr0.2Ti0.8)O3 – 0.5(Ba0.7Ca0.3)TiO3 Thin Films Prepared by a Sol-Gel Process. *J. Phys. Chem. C* **118,** 15220–15225 (2014).

37. Gao, H. *et al.* Structure and magnetic properties of three-dimensional (La,Sr)MnO[sub 3] nanofilms on ZnO nanorod arrays. *Appl. Phys. Lett.* **98,** 123105 (2011).

38. Zheng, H. *et al.* Self-Assembled Growth of BiFeO3–CoFe2O4 Nanostructures. *Adv. Mater.* **18,** 2747–2752 (2006).

FERROMAGNETIC RESONANCE STUDY OF BZT-BCT/ LSMO HETEROSTRUCTURE GROWN ON DIFFERENT SUBSTRATES-LAO AND PLATINUM USING PULSED LASER DEPOSITION

Abstract

In this article, dynamic magnetic properties of $La_{0.7}Sr_{0.3}MnO_3$ (LSMO) capped with a Pb-free ferroelectric BZT-BCT layer deposited on two different substrates lanthanum aluminate (LAO) and Platinum (Pt) by pulsed laser deposition (PLD) have been investigated by FMR spectroscopy. The thin films on LAO substrate were highly (00l)-oriented whereas for Pt substrate, the films were randomly oriented. XRD data confirm the epitaxial growth of the thin films. The vibrational modes of the ferroelectric layer, investigated through Raman spectra, reveal significant red shifts for the thin films on Pt substrate compared to films on LAO substrate. The well-behaved room temperature M-H curves were observed for all the films through superconducting quantum interference device (SQUID) magnetometer indicating the ferromagnetic behavior of LSMO. The right shift of the hysteresis loop of the heterostructure may arise from the ME coupling between the ferroelectric and ferromagnetic layers. FMR measurement yields the significant values of linewidth offset, Gilbert damping parameter, gyromagnetic ratio, and in-plane uniaxial anisotropy field of the thin films. We found the lowest Gilbert damping parameter 0.02883 for the heterostructure BZT-BCT/LSMO/ LAO. In addition, the gyromagnetic ratio was also found lowest (0.00169 GHz/Oe) for the same film. The analysis concludes possible spintronic applications using BZT-BCT/LSMO on LAO substrate rather than films on Pt substrate.

Introduction

The precursor material of LSMO is lanthanum manganite ($LaMnO_3$). After doping Sr^{2+} into $LaMnO_3$ through solid-state reaction, LSMO is formed and it shows some amazing properties far away from $LaMnO_3$. The unique properties are promising for potential applications in magnetic, magnetoelectronic, and photonic devices as well as in infrared detector and spintronic technology. The interplay among the spin, charge, and orbital degrees of freedom in this material[1] leads to many intriguing phenomena such as metal-insulator transition, magnetic phase transition, and nanoscale electronic phase separation[2].

LSMO belongs to the family of perovskite like mixed valence manganites which is the most studied colossal magnetoresistant (CMR) material. The half-metallic nature of LSMO yields a high-spin polarization of its conducting electrons. This property makes it a reliable material for spin-dependent transport devices such as spin valves[3], magnetic tunneling junctions[4] especially when it is grown on strontium titanate (SrTiO3 or STO) and neodymium gallate (NdGaO3 or NGO) substrates. LSMO has nearly 100% spin polarization and a high Curie temperature of 365k. The other applications of LSMO involve magnetic random access memory (MRAM), read heads in hard disk drives, as well as spin-logic based devices[5]. Moreover, there are more advanced applications of magnetic materials in data transfer in magnetic recording systems. The switching speed of the magnetic elements for those applications is limited, in part, by the magnetic damping in the thin film. An understanding of the damping mechanisms and control parameters remains one of the key challenges in the push to achieve faster switching speeds. In this respect, it is a must to understand the magnetic dynamics and to tune the

damping properties of LSMO for realizing high-speed spintronic devices. The damping constant determines the critical switching current in a spin-torque transfer (STT) based devices[6]. For STT based MRAM, damping constant must be small to minimize the power consumption. Also, for TMR read heads, the thermal magnetic noise depends on the damping parameters which affects SNR of a read head[7]. On the other hand, a large damping constant is expected for the read sensors to improve the thermal stability[8].

All the above mentioned applications required LSMO interfaced with either an insulator or conducting or semiconducting materials. But the properties of LMSO is changed due to the interface and it makes the device applications limited[9]. In that respect, understanding the surface and interface properties of LSMO for magnetic and transport mechanism is vital. The properties of LSMO interfaced with a ferroelectric material is promising for various applications. Specially, how the magnetization of an LSMO thin film is altered when epitaxially joined to a ferroelectric material is very important. Interface surface pinning, unidirectional and uniaxial anisotropies and changes to other micromagnetic properties are all key characteristics for tunnel junction performance. Several reports demonstrated these properties in single-layer LSMO[10]. The effects of ferroelectric overlayer can be important and have begun to be studied[11]. In this report, we have shown the FMR study of LSMO thin film deposited on different substrates-LAO and Pt. Also, we have demonstrated the change of FMR properties after interfacing with a ferroelectric material BZT-BCT. The low values of Gilbert damping parameter with the typical values of gyromagnetic ratio and in-plane uniaxial anisotropy field confirm the possible applications in high-speed spintronic devices.

Experimental

All chemicals were analytic grade reagents and used without further purification. The BZT-BCT ceramic target was prepared by a standard solid state reaction using high purity chemicals $BaCO_3$ (99.9%, Inframat Advanced Materials), CaO (99.95%, Alfa Aesar), TiO_2 (99.9%, Sigma-Aldrich), and ZrO_2 (99.9%, Inframat Advanced Materials) in appropriate proportions. Polyvinyl Alcohol (PVA) was added to the mixture to prevent agglomeration of the powder particles. The final mixer was pressed with a 'hydraulic press' to form the target. After that, the prepared target was calcined at 1350^oC and then sintered at 1450^oC in the air. The CFO target was prepared from $CoFe_2O_4$ nanopowder (Inframat Advanced Materials) applying the same procedure with 900^oC sintering temperature. On the other hand, a high purity dense Lanthanum Strontium Manganite ($La_{0.7}Sr_{0.3}MnO_3$) (LSMO) target was purchased from Kurt J. Lesker Company. The target was 99.9% pure, 1.00" diameter×0.250" thick, +/-0.010" AL.

A CMP polished highly oriented (001) LAO substrate (2" dia +/- 0.5 mm × 0.5 thickness +/-0.05 mm) was purchased from MTI Corporation. The configuration of the substrate was as follows: surface finish (RMS or Ra): < 8A with free sub-surface damaged, under 1000 class clean room, and in 100 grade plastic bag in a wafer container. The platinum substrate was also bought from MTI corporation with following specifications: Film-SiO_2+Ti+Pt (111) thin film on Si (100) (P-type) substrate, 2"x0.279mm, 1 side polished (1sp), SiO_2=300 nm, Ti=10 nm, Surface roughness: < 20 A RMS.

All the thin films were deposited on LAO and Pt substrate by Pulsed Laser Deposition (Excel Instrument, PLD-STD-18) technique using those targets. A KrF

excimer laser (Lambda Physik, COMPEX 201) with an energy density of 2 Jcm^{-2}, wavelength 248 nm, pulsed duration of 20 ns, was used with 10 Hz pulse rate for the deposition. Thin films were grown in different growth temperature (600^0C to 850^0C) and different oxygen pressure (10^{-1} to 10^{-4} mbar). The best performance was observed in the film grown at the growth temperature of 800°C with 4.1×10^{-1} mbar oxygen pressure. The base pressure of the chamber was maintained at 9×10^5 mbar. After the desired number of PLD shots, the deposited film was cooled down to room temperature maintaining the oxygen pressure at 110 mbar. The average film thickness was 100 nm, measured ex-situ by a profilometer (Veeco, Dektak 150).

Thin films were characterized by X-ray Diffractometer (Bruker, D8 Discover) using θ-2θ scan in the range of 20° to 80° maintaining the Bragg−Brentano reflection geometry. The excitation source was an x-ray with the wavelength of 1.5405Å. The vibrational properties of the samples were characterized by micro-Raman scattering experiments (Horiba Labram Raman-PL System) with a 532 nm green laser excitation source. The experiments were performed in a back-scattering geometry with 15 seconds exposure time, and 20 accumulation cycles. The measured spot size was approximately 2.5 μm in diameter on the thin film. We were aware of the possible damage of the thin film due to the excitation source. The Raman spectroscopy was collected through NGS Labspec-5 software in the range of 100 cm^{-1} to 1000 cm^{-1}. The data were analyzed by Gaussian-Lorentzian peak fitting using Origin Pro 8.5.1.

The magnetization of the films was measured by SQUID mangnetometer (Quantum Design MPMS 5XL) interfaced through MultiVu software. The temperature was varied from 5k to 370k. Low temperature (5k) and high temperature (300k) M-H

hysteresis loop of the sample was observed by varying the magnetic field from -5000 Oe to +5000 Oe. The maximum sensitivity of the magnetometer was 10^{-9} emu. In our experiment, we used a slow and steady temperature ramp and sent a constant current using the current source.

Results and Discussion

Figure 10 illustrates the XRD pattern of both the BZT-BCT/LSMO (black) and only LSMO (red) thin films on LAO substrate. The XRD pattern shows the highly-oriented spectra which are the indication of a complete single phase perovskite structure. Puli et al. demonstrated a possible secondary phase such as $Ba_3Ca_2Ti_2O_9$ in the (1-x) BZT-xBCT ceramic system[12]. But in our sample the existence of any secondary phases is ruled out due to sintering at a higher temperature. Also, the complete solid solubility of

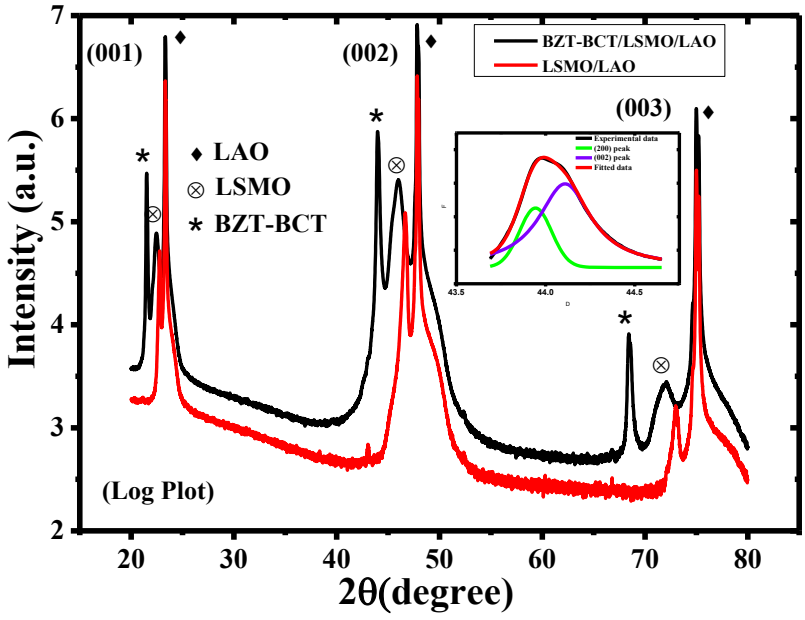

Figure 10. X-ray diffraction pattern of both LSMO (red line) and BZT-BCT/LSMO (black line) on LAO substrate. The inset plot shows the splitting of (002) peak, which is a characteristic of the tetragonal crystal structure.

Ca^{2+} at Ba-site and Zr^{4+} at Ti-site at higher sintering temperature ruled out the possibility of any impurities, confirmed by XRD.

The interesting feature of the XRD pattern is the splitting of the peaks. The inset of Figure 10 shows that weak splitting of the XRD peak in the 2θ range of 43.5 to 44.5 induced by the formation of multiple domains, e.g., a- and c-domains, analogous to the case of PZT[13]. This is a unique characteristic of the tetragonal phase in BZT-BCT as the single (002) plane (cubic phase) transforms to (200) and (002) crystallographic planes (tetragonal phase). The other interesting feature of the XRD is the asymmetricity of the peak shape which confirms the coexistence of tetragonal and cubic phases in our thin film. The average ⟨111⟩ displacements of octahedral Ti^{4+} (local rhombohedral structure) is the reason of the tetragonal structure[14]. The presence of CuK_α or CuK_β at higher angles can't be the source of the peak splitting as this is predominantly seen in the mentioned 2θ range. The other diffraction peak (003) at 68.5^o also shows mixed diffraction peaks, which is consistent with Liu's report[15]. Such coexistence plays a key role in enhancing the ferroelectric performance of BZT-BCT.

The *c*-axis lattice constants, of LSMO, calculated from the XRD data for LSMO/LAO and BZT-BCT/LSMO/LAO are 3.892 and 3.943 Å respectively. As the lattice constant of bulk LSMO is 3.889 Å, this induces tensile strain in the LSMO thin film. However, the scenario is critical for the heterostructure. The BZT-BCT/LSMO/ LAO heterostructure experiences two strain effects, one incurred from the strain of LSMO/LAO due to the lattice mismatch between the film and the substrate and the other from the BZT-BCT/LSMO interface.

Figure 11 represents the XRD pattern of the LSMO thin film grown on Pt substrate, which reveals the randomly oriented nature of the film. The XRD peaks at 23.04, 32.5, 47.5, and 69.83 correspond to LSMO (001), LSMO (011), LSMO (002), and LSMO (003) respectively. The other peak at 40.03 denotes the reflection from Pt substrate.

To investigate the molecular vibrational modes present in the sample, we performed room-temperature Raman experiment. This spectroscopy is a highly sensitive technique to evaluate the atomic structure and phases of perovskite BZT-BCT. ABO_3 type perovskite structures are very interesting to investigate. For example, Raman active modes are only found in the tetragonal perovskite structure rather than in cubic structure[16]. $BaTiO_3$ (BTO), a perovskite, is the primary material of the BZT-BCT composite. There are fifteen degrees of freedom present per unit cell (uc) of tetragonal BTO as it has five atoms in a uc[17]. The transition temperature (T_t) of BTO is 120°C. The

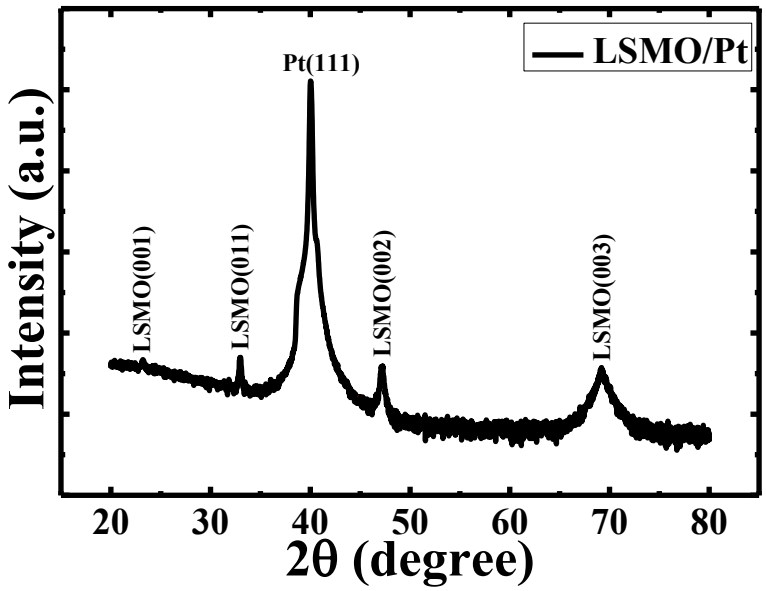

Figure 11. X-ray diffraction pattern for PLD grown LSMO thin film on Pt substrate

tetragonal crystal structure of BTO transforms to cubic crystal structure upon heating above T_t. In addition, the ferroelectric property vanishes at this temperature. The cubic BTO is not Raman active while the tetragonal structure shows significant modes[18]. Figure 12(a) shows the following six active modes in Raman spectra of the BZT-BCT/LSMO thin film on both the LSMO and Pt substrate: 2 A_1(TO), 1 A_1(LO), 1 E(TO), 1 E(LO), and 1 B_1. Due to the presence of long-range electrostatic forces[19] each of the A_1 and E modes split into TO (transverse optical) and LO (longitudinal optical) modes. Figure 12(b) represents the deconvolution of the vibrational modes of BZT-BCT.

The peaks in the BZT-BCT thin film on both the substrates are observed near 175, 300, 525, and 735 cm^{-1}. The peak near 175 cm^{-1} represents the Ti-O phonon vibrations of BZT-BCT and denoted to the A_1(TO) mode[20]. Another A_1(TO) mode at near 525 cm^{-1} represents the O-Ti-O symmetric stretching vibrations[21]. The first-order Pm3m Raman scattering is symmetry-forbidden in the centrosymmetric space group. So, due to a Ti or

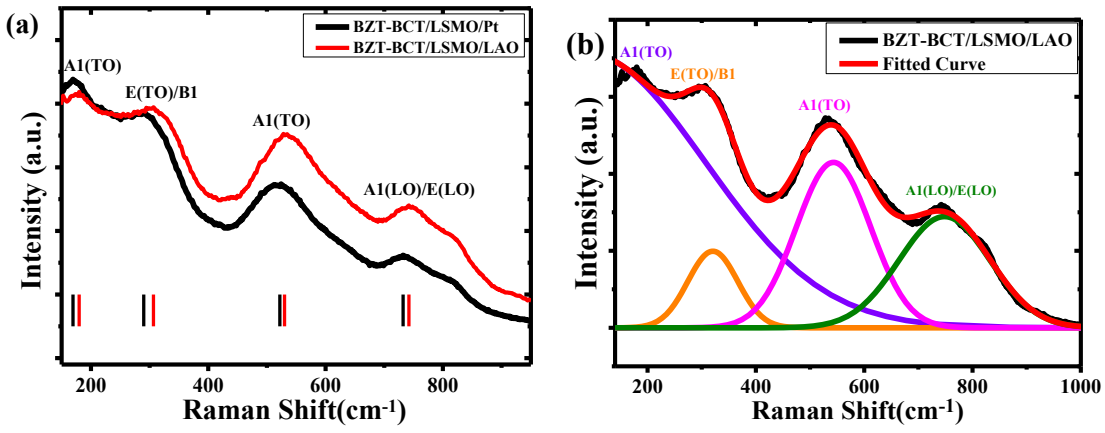

Figure 12. Raman spectra of PLD grown thin films (a) BZT-BCT/LSMO on Pt substrate (black line), BZT-BCT/LSMO on LAO substrate (red line) and (b) Deconvolution of Raman spectra with Gaussian and Lorentzian peak fitting by using Origin Pro 8.5.1

Zr atom's displacement from its octahedral position, the presence of non-centrosymmetric regions yield the symmetric stretching vibrations[22]. The sharp feature of the peak near 525 cm^{-1} indicates the high quality of the thin film. The characteristic peak for BZT–BCT, near 300 cm^{-1}, is attributed to the B_1 mode. This mode indicates the asymmetry of the TiO_6 octahedra[23]. This band is also considered to be the Raman signature of the tetragonal phase. The A_{1g} octahedral breathing mode at 800 cm^{-1} which is absent in the Raman spectra which confirm that Ca^{2+} resides on Ba-site not Ti-site in our cases[24].

A_1 (LO) vibrational mode near 735 cm^{-1} is quite broad and shifted compared to its bulk counterpart. This is a characteristic feature of the tetragonal phase in thin films. The broadening represents the distortion in the thin film while the peak shift is related to the non-centrosymmetric region in the unit cell. Some of the Raman modes in our sample are weak due to heavily damped phonons.

The BZT-BCT thin films in our study were epitaxially grown on conducting oxide (LSMO), which was earlier grown on different substrates (Pt and LAO). The LAO substrate is insulating while the Pt one is conducting. So, in the sample BZT-BCT/ LSMO/Pt, obviously, the vibrational modes originate from the top BZT-BCT layer. Also, in the sample BZT-BCT/LSMO/LAO, the conducting LSMO reflects the exciting laser beam so that it does not enter the LAO substrate. Actually, this kind of heterostructure has several advantages. First, the conducting layer doesn't allow the laser to enter into the substrate. Therefore, the Raman signal is exempt of the substrate. Second, the conducting oxide bilayer ensures the high quality epitaxial growth of the ferroelectric thin film in comparison to Si, sapphire substrates. Furthermore, such bilayer structures are similar to

those used in tunable microwave devices which make the experimental results more relevant to practical applications.

Both the thin films were grown following exactly the same deposition parameters and both the Raman spectra denote vibrational modes of BZT-BCT. However, we found red shifts in each of the Raman peaks for the sample grown on Pt substrate compared to LAO substrate. These shifts caused by the substrate can come from several sources including surface charge, surface adhesion, defects, chemical environments and/or strain. As the same techniques were applied throughout deposition, the deviation of chemical composition can be ruled out. In addition, the surface charge and surface adhesion can be canceled due to the same oxide layer on both substrates. Therefore, the epitaxial strain originating from the substrate is responsible for the shifting of Raman modes. The BZT-BCT film on LAO substrate was highly oriented along (00l) crystallographic plane whereas on Pt Substrate it was polycrystalline. The polycrystalline film is fully constrained by the Pt substrate, resulting in the large in-plane compressive strain. On the other hand, the (00l)-epitaxial film is almost fully relaxed. Table 5 shows the vibrational modes of BZT-BCT thin films grown on Pt and LAO substrates.

The high-quality of the BZT-BCT thin films are confirmed by the well-defined Raman spectra. Taken together, Raman and XRD indicate the presence of non-centrosymmetric regions that result from the local off-centering of the titanium (zirconium) atoms.

PLD-grown LSMO thin film was highly epitaxial stimulated by monocrystalline LAO substrate at higher deposition temperature. Figure 13(a) (red) shows the M-H curve

Table 5. Peak positions and FWHM of the corresponding vibrational modes observed in Raman spectroscopy of BZT-BCT/LSMO thin films on Pt and LAO substrates

Peak Position (cm^{-1})		Amount of Peak shift (cm^{-1})	Vibration mode
Pt Substrate	LAO Substrate		
169.33	179.94	10.61	A_1(TO)
290.04	306.68	16.64	E(TO)/B_1
524.16	528.30	4.14	A_1(TO)
732.15	742.05	9.9	A_1 (LO)/E(LO)

of LSMO/LAO thin film with the field applied parallel to the film plane at room temperature. Figure 13(b) shows the low field fragments of the hysteresis loops of Figure 13(a). The magnetization was calculated after subtraction of a diamagnetic background from the substrate. The magnetization increased with increasing magnetic field until the saturation was reached at 500 Oe. A well-behaved M-H curve was observed for the

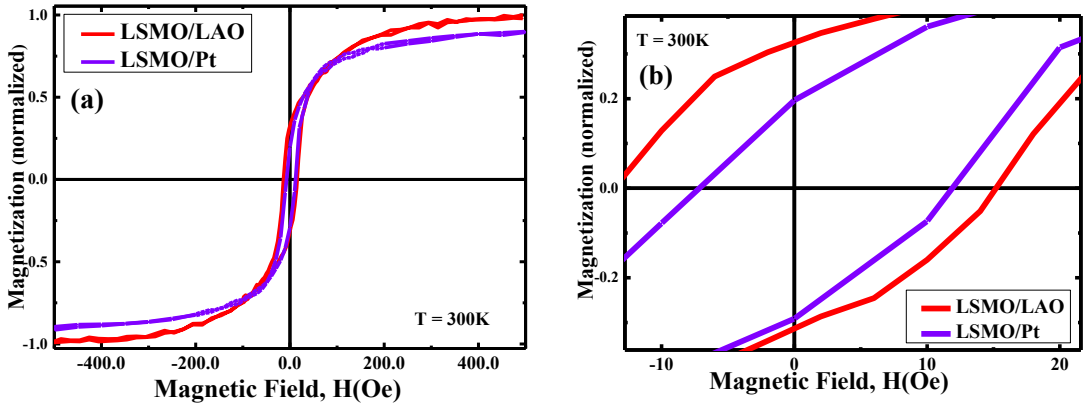

Figure 13. (a) Magnetization-Applied field (M-H) hysteresis loop of the LSMO/LAO (red), LSMO/Pt (purple) obtained at room temperature and (b) the low field fragments of the hysteresis loops of Figure (a)

LSMO thin film, which is the indication of ferromagnetism in the sample. The film exhibited a coercive field of 15.2 Oe and a squareness ratio of 0.34.

On the other hand, LSMO thin film on Pt substrate was randomly oriented. Figure 13(a) (purple) shows the M-H curve of LSMO/Pt thin film. The magnetization increases with increasing magnetic field until the saturation is reached at a high field of 1000 Oe. A well-behaved M-H curve indicates the ferromagnetism in the sample. The film exhibits a coercive field of 11.9 Oe and a squareness ratio of 0.2.

The LSMO thin film on LAO substrate is superior to the film on Pt substrate for different applications. Both the coercive field and the squareness ratio are much larger for LSMO/LAO than LSMO/Pt. In addition, a high saturation field for LSMO/Pt indicated that the sample is magnetically hard than LSMO/LAO.

Figure 14(a) (red) shows the M-H curve of BZT-BCT/LSMO/LAO thin films with the field applied parallel to the film plane at room temperature. Figure 14(b) shows the low field fragments of the hysteresis loops of Figure 14(a). The magnetization increased with increasing magnetic field until the saturation was reached at 500 Oe. A well-behaved M-H curve indicates the ferromagnetism in the sample. The film exhibits a coercive field of 4.45 Oe and the squareness ratio of 0.08.

On the other hand, Figure 14(a) (green) shows the M-H curve of BZT-BCT/ LSMO/Pt thin film with the field applied parallel to the film plane at room temperature. The magnetization increases with increasing magnetic field until the saturation is reached at a high field of 5000 Oe. The film exhibits a coercive field of 2.51 Oe and the squareness ratio of 0.075.

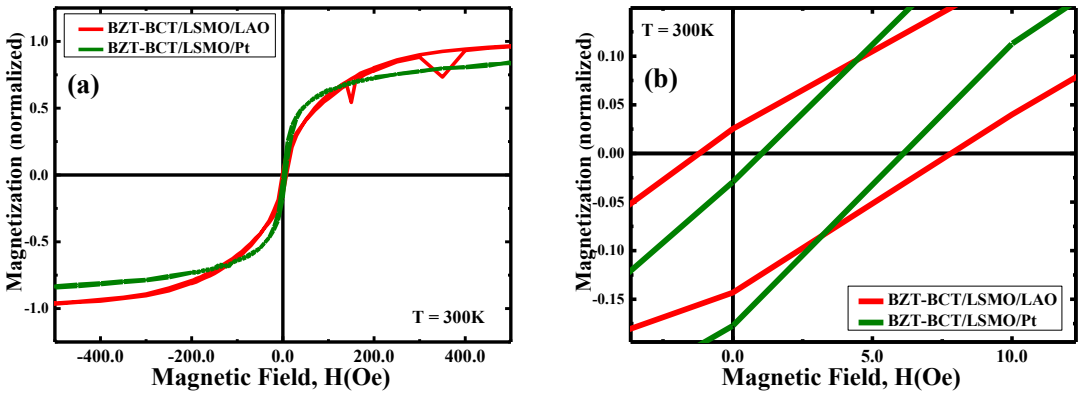

Figure 14. (a) Magnetization-Applied field (M-H) hysteresis loop of the BZT-BCT/ LSMO/LAO (red), BZT-BCT/LSMO/Pt (green) obtained at room temperature and (b) the low field fragments of the hysteresis loops of Figure (a)

The coercive field is much larger for BZT-BCT/LSMO/LAO than BZT-BCT/LSMO/Pt. However, the squareness ratios are almost same. In addition, a high saturation field for BZT-BCT/LSMO/Pt indicates that the sample is magnetically hard than the other sample. Table 6 summarizes values from SQUID measurement.

The FMR measurements were carried out using a microwave cavity at a wide range of frequencies with a static magnetic field applied parallel to the film plane. The resonance condition in this configuration is given by

Table 6. Static Magnetic properties derived from SQUID measurement for all the samples

Sample:	LSMO/LAO	LSMO/Pt	BZT-BCT/ LSMO/ LAO	BZT-BCT/ LSMO/Pt
Coercive field, H_c (Oe)	15.19	11.90	4.45	2.51
Squareness Ratio, M_r/M_s	0.341	0.199	0.08	0.075
Saturation Field, M_s(Oe)	500	1000	500	5000

$$f = \gamma\sqrt{(H_r + H_k)(H_r + H_k + 4\pi M_s)} \quad \text{----------(1)}$$

where f is the FMR frequency, γ is the gyromagnetic ratio, H_k is the in-plane uniaxial anisotropy field, $4\pi M_s$ is the saturation magnetization, and H_r is the resonance magnetic field. The other important parameter is 'FMR linewidth', which is a sensitive probe for providing magnetic homogeneity in the thin film. The temperature independent and narrower linewidths are the signature of the homogeneous sample.

Figure 15(a) shows the experimental FMR absorption derivative versus field profiles at integral frequencies between 7 and 9 GHz for LSMO/LAO thin film. It is remarkable to note that the film displays pronounced ferromagnetic resonance at room temperature. The FMR signal is nearly symmetric but there is a little bit distortion at the field far away from resonance field on both sides. Though the absorption mode strength was strongest near 7 GHz, the intensity does not vary so much at other frequencies. That means the magnetization of the sample does not affect by the microwave excitation. The horizontal line is the zero-mark and the resonant field (H_r) was calculated from the first zero-crossing of the differential power absorption before going minimum. The resonant fields were 1163 to 1730 Oe at different frequencies depending on the excitation source. It shifts towards higher values as the excitation frequency increases. The linewidths (ΔH) were calculated from the maximum and minimum of the absorption derivative and the values were 180 to 200 Oe. Figure 15(b) shows frequency dependent in-plane linewidth of LSMO/LAO sample. The curve shows a linear fit of the LLG approach[25] described by the following equation:

$$\Delta H(f) = \Delta H_0 + \frac{2\alpha}{\gamma\sqrt{3}} f \qquad (2)$$

where ΔH(f) is the linewidth at frequency f, ΔH_0 is the linewidth offset at zero frequency caused by microstructural inhomogeneities and α is the Gilbert damping parameter. The linear fit yields a linewidth offset of 34.86 Oe, which is lower than the recently reported value (541.45 Oe for LSMO/STO). The small value of ΔH_0 confirmed the homogeneity of the sample. Figure 15(c) shows the frequency dependence of FMR resonant field for a wide range of frequencies. The curve was fitted to the Kittel resonance equation. The slope of the linear fit was 0.003 which demonstrated the value of the gyromagnetic ratio

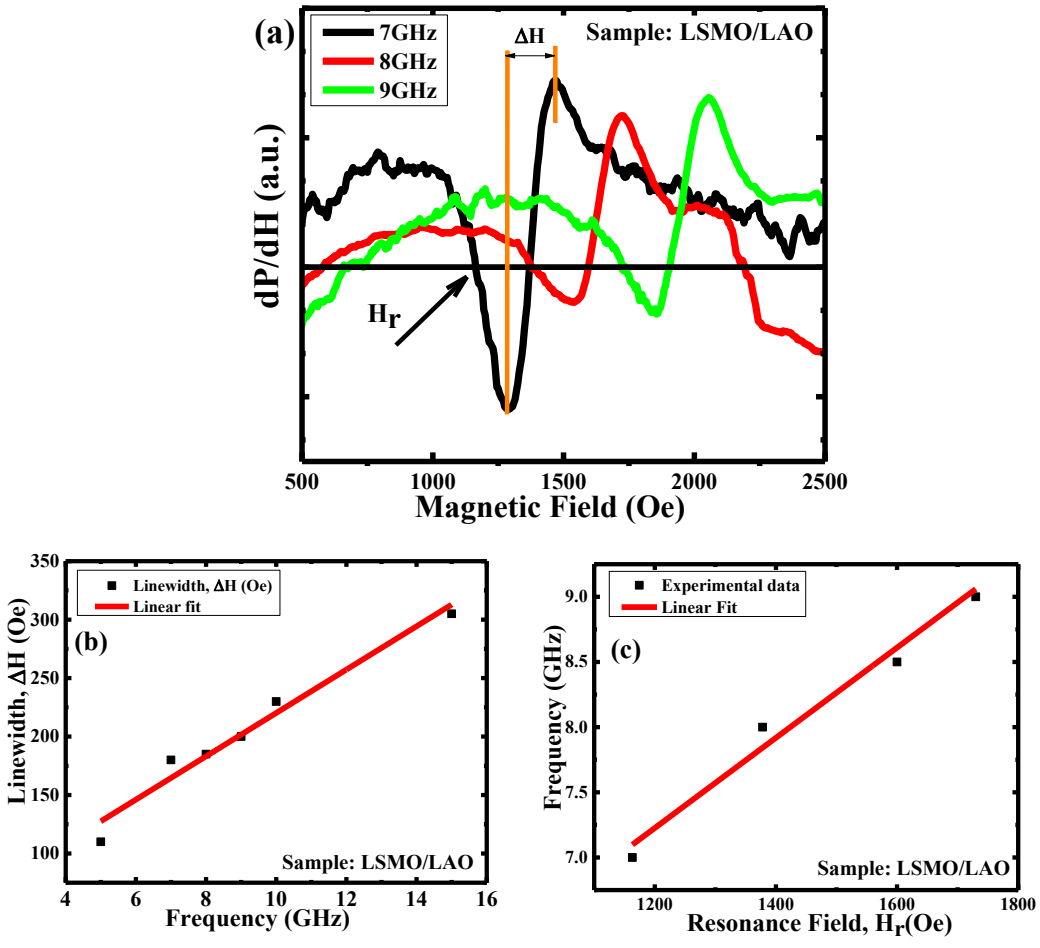

Figure 15. (a)FMR absorption derivative vs applied magnetic field for the sample LSMO/LAO at 7 GHz (black), 8 GHz (red), and 9 GHz (green). The arrow shows the resonant frequency and the width (orange line) shows the linewidth. (b) Frequency dependence of FMR linewidth and (c) FMR resonance field for the same sample.

of the magnetic thin film. The Gilbert damping parameter was calculated 0.037 and the in-plane uniaxial anisotropy field was found 1099.7 Oe.

Figure 16(a) shows the experimental FMR absorption derivative versus field profiles at integral frequencies between 8 and 9.5 GHz for LSMO/Pt thin film. The film displays a large ferromagnetic resonance at room temperature. The FMR signal at higher frequencies showed some distortion. The resonant fields were 1500 to 2000 Oe at different frequencies depending on the excitation source. The linewidths (ΔH) of the absorption derivative were between 250 to 300 Oe. Figure 16(b) shows frequency dependent in-plane linewidth of LSMO/Pt sample. The curve shows a linear fit of the LLG approach described by equation (2) which yields a linewidth offset of 187.09 Oe. The small value of ΔH_0 confirmed the homogeneity of the sample.

Figure 16(c) shows the frequency dependence of FMR resonant field for a wide range of frequencies. The curve was fitted to the Kittel resonance equation, which yields a value of 0.0038 for the gyromagnetic ratio. The Gilbert damping parameter was calculated 0.05 and the in-plane uniaxial anisotropy field was found 126.6 Oe.

Figure 17(a) shows the experimental FMR absorption derivative versus field profiles at integral frequencies between 7 and 9 GHz for BZT-BCT/LSMO/LAO thin film. The film displays a large ferromagnetic resonance at room temperature but shows some distortion far away from resonance. The resonant fields were 1300 to 2000 Oe at different frequencies. The linewidths of the absorption derivative were between 115 to 145 Oe. Figure 17(b) shows the frequency dependent in-plane linewidth of BZT-BCT/ LSMO/LAO sample. The curve shows a linear fit of the LLG approach described by equation (2) which yields an offset of 48.17 Oe. The small value of ΔH_0 confirmed the

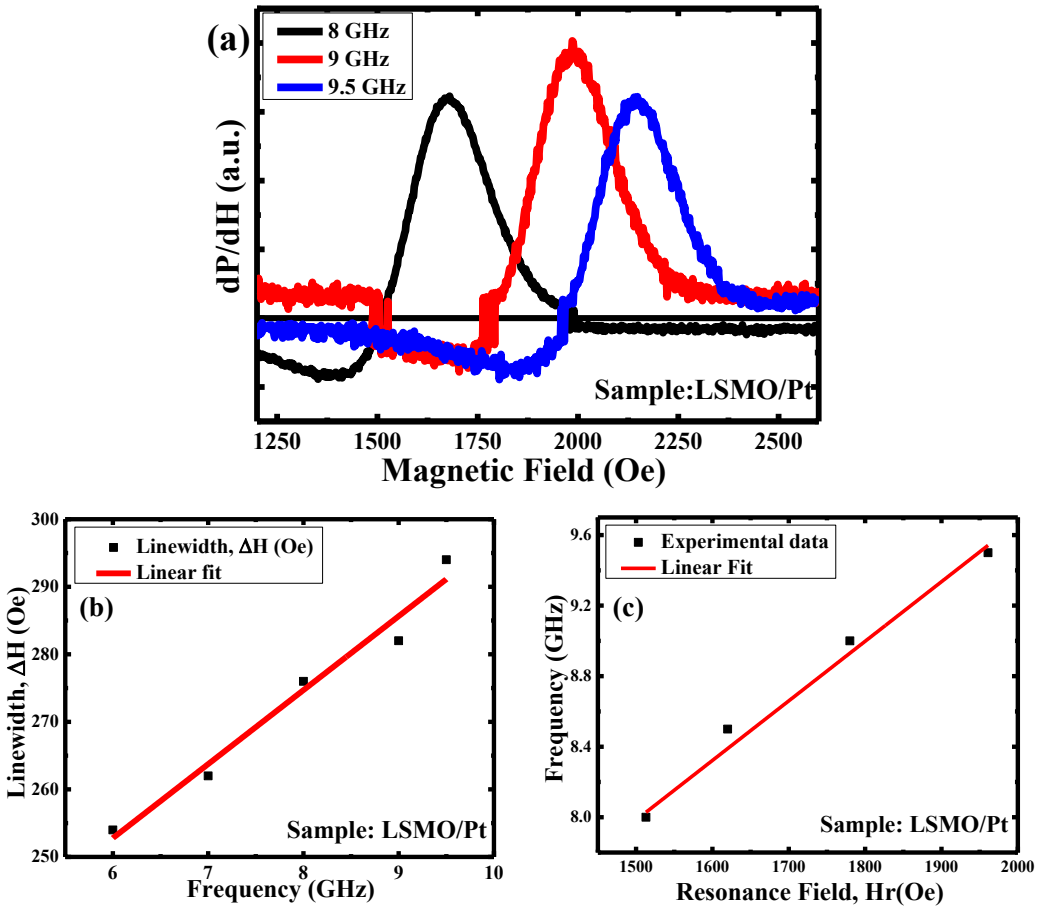

Figure 16. (a) FMR absorption derivative vs applied magnetic field for the sample LSMO/Pt at 7 GHz (black), 8 GHz (red), and 9.5 GHz (blue). The arrow shows the resonant frequency and the width (orange line) shows the linewidth. (b) Frequency dependence of FMR linewidth and (c) FMR resonance field for the same sample

homogeneity of the sample. Figure 17(c) shows the frequency dependence of FMR resonant field for a wide range of frequencies. The curve was fitted to the Kittel resonance equation, which yields a value of 0.00169 for the gyromagnetic ratio. The Gilbert damping was calculated 0.02883 and the uniaxial anisotropy field was found 347.1 Oe.

Figure 18(a) shows the experimental FMR absorption derivative versus field profiles at integral frequencies between 7 and 9 GHz for BZT-BCT/LSMO/Pt thin film.

The film displays some distortion at all frequencies. The resonant fields were 400 to 1800 Oe at different frequencies. The linewidths (ΔH) of the absorption derivative were between 290 to 360 Oe. Figure 18(b) shows the frequency dependent in-plane linewidth of BZT-BCT/LSMO/Pt sample. The curve shows a linear fit of the LLG approach described by equation (2) which yields a linewidth offset of 120.9 Oe. The small value of ΔH_0 confirmed the homogeneity of the sample. Figure 18(c) shows the frequency dependence of FMR resonant field for a wide range of frequencies. The curve was fitted

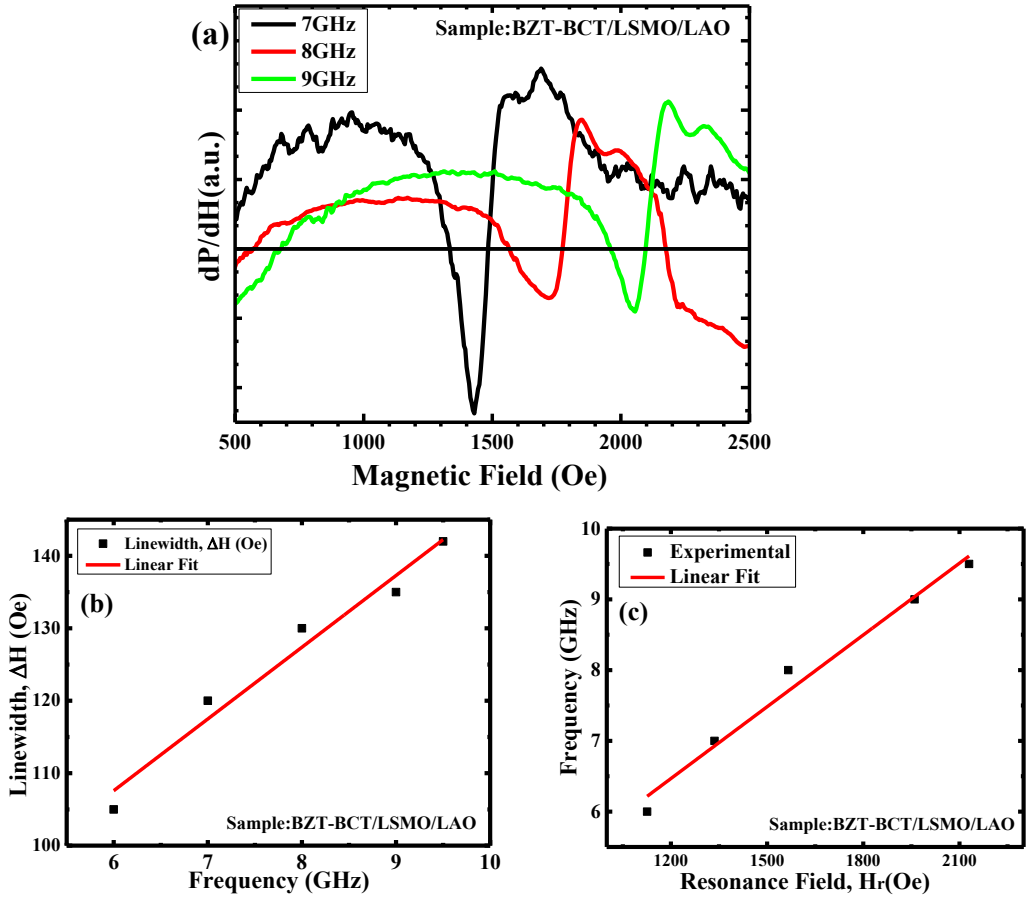

Figure 17. (a)FMR absorption derivative vs applied magnetic field for the sample BZT-BCT/LSMO/LAO at 7 GHz (black), 8 GHz (red), and 9 GHz (green). The arrow shows the resonant frequency and the width (orange line) shows the linewidth. (b) Frequency dependence of FMR linewidth and (c) FMR resonance field for the same sample.

to the Kittel resonance equation that yields a value of 0.00338 for the gyromagnetic ratio. The Gilbert damping parameter was calculated 0.0376 and the in-plane uniaxial anisotropy field was found 23.3 Oe.

For the sample LSMO/LAO the linewidth-offset, Gilbert damping parameter, and saturation magnetization are quite small compared to LSMO/Pt sample. In addition, a high squareness ratio and high in-plane anisotropy field for the LSMO/LAO sample confirmed its superiority than LSMO/Pt.

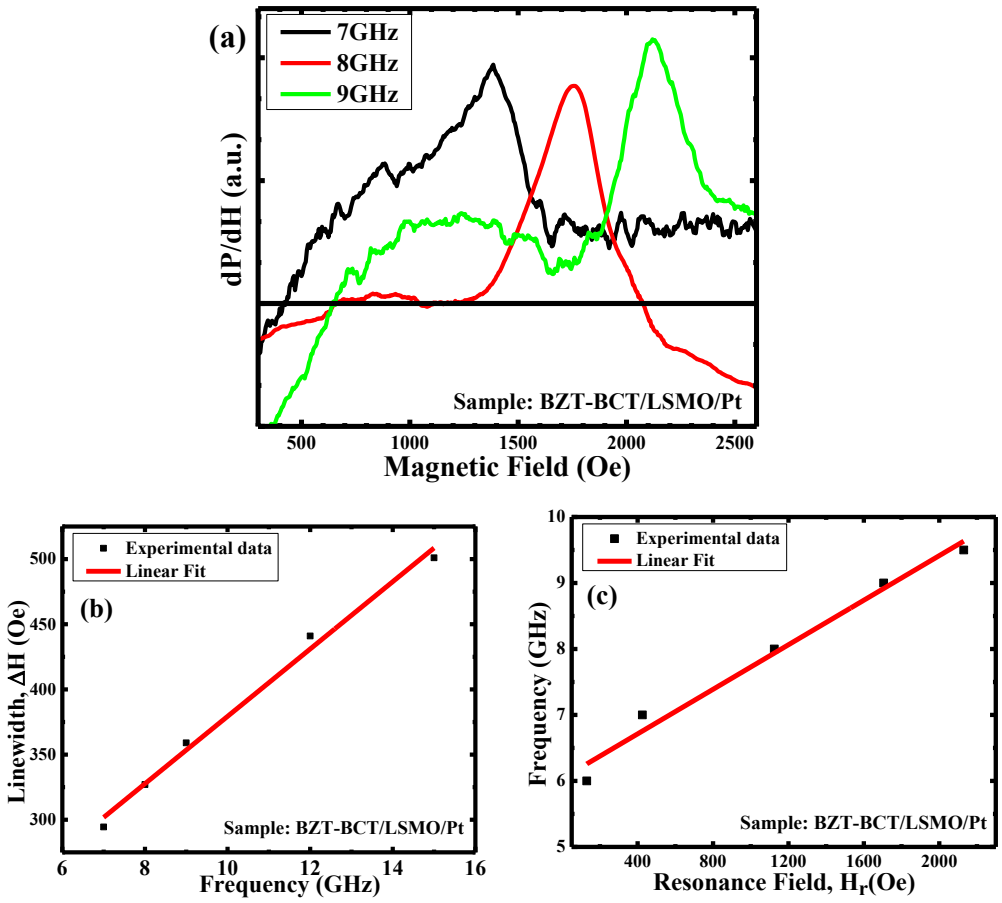

Figure 18. (a) FMR absorption derivative vs applied magnetic field for the sample BZT-BCT/LSMO/Pt at 7 GHz (black), 8 GHz (red), and 9 GHz (green). The arrow shows the resonant frequency and the width (orange line) shows the linewidth. (b) Frequency dependence of FMR linewidth and (c) FMR resonance field for the same sample.

For the sample, BZT-BCT/LSMO deposited on LAO substrate, the linewidth-offset, Gilbert damping parameter, and saturation magnetization is quite small compared to film on Pt substrate. In addition, the high in-plane anisotropy field for the BZT-BCT/LSMO/ LAO sample confirmed its superiority than BZT-BCT/LSMO/Pt. However, the squareness ratio was almost same for both the sample.

The effect of an FE layer capping to the sample LSMO/LAO can be revealed from the above FMR absorption derivatives. After capping with an FE layer the linewidth-offset increases a little bit whereas the Gilbert damping parameter, squareness ratio, and anisotropy field decrease. On the other hand, the saturation magnetization of LSMO capped with an FE layer increases a lot indicating that a high field is necessary to reorient the magnetic field. However, after capping with an FE layer all the parameters except the saturation magnetization decreased. The saturation magnetization increases almost three times indicating that a high field is necessary to reorient the magnetic field. All the calculated values from the FMR measurements were presented in Table 7.

Table 7. Dynamic magnetic properties of all the samples calculated from FMR

Sample:	LSMO/LAO	LSMO/Pt	BZT-BCT/ LSMO/LAO	BZT-BCT/ LSMO/ Pt
Linewidth offset, ΔH_0 (Oe)	34.86	187.09	48.17	120.9
Gilbert damping parameter, α	0.037	0.05	0.02883	0.0376
Gyromagnetic ratio,(GHz/Oe)	0.003	0.0038	0.00169	0.00338
Saturation magnetic field, Oe	500	1000	500	5000
Uniaxial anisotropy, H_k (Oe)	1099.7	126.6	347.1	23.3

Conclusions

Both the BZT-BCT and LSMO thin films on LAO were highly oriented stimulated by the monocrystalline substrate. On the other hand, the pseudo-crystalline Pt substrate yield randomly oriented thin films. The red shifts of the Raman vibrational peaks of BZT-BCT originate from the strain of Pt/LSMO interface. The well-behaved M-H hysteresis loops confirm the ferromagnetic behavior of all the LSMO thin films. The observed right shift of the hysteresis loops of LSMO in presence of an FE top layer may be an indication of the desired magnetoelectric coupling between the FE and FM layers. The advanced applications depend upon this kind of coupling between two different materials. Thin films on Pt substrate are magnetically hard than the films on LAO substrate. However, FMR data reveal the dynamic magnetic properties of PLD grown thin films. Thin films deposited on LAO substrate show the lowest linewidth offset compared to the films on Pt substrate. The Gilbert damping parameter and the gyromagnetic ratio are smaller for the thin films on LAO substrate indicating possible applications mentioned in the earlier sections such as MRAM, data storage, high-speed switching sensors, actuators etc. Moreover, the in-plane anisotropy fields are much higher for the films on LAO than the films on Pt indicating strong anisotropy in LSMO/LAO. On the other hand, the dynamic behavior of LSMO/LAO thin film is quite similar to the same thin film with the top ferroelectric layer. But, the dynamic properties of LSMO/Pt change a lot with FE top layer. So, we can conclude that LSMO thin film can be joined with another ferroelectric layer for device applications when the insulating substrate or some insulating layer is necessary for isolation. More study on interface behavior and charge transport mechanism are needed to bolster above statements.

References

1. Tokura & Nagaosa. Orbital physics in transition-metal oxides. *Science* **288,** 462–468 (2000).

2. Loudon, J. C., Mathur, N. D. & Midgley, P. A. Charge-ordered ferromagnetic phase in La(0.5)Ca(0.5)MnO3. *Nature* **420,** 797–800 (2002).

3. Xiong, Z. H., Wu, D., Valy Vardeny, Z. & Shi, J. Giant magnetoresistance in organic spin-valves. *Nature* **427,** 821–824 (2004).

4. Ishii, Y. *et al.* Perovskite manganite magnetic tunnel junctions with enhanced coercivity contrast. *Appl. Phys. Lett.* **87,** 22509 (2005).

5. Yoda, H. *et al.* High efficient spin transfer torque writing on perpendicular magnetic tunnel junctions for high density MRAMs. *Curr. Appl. Phys.* **10,** e87–e89 (2010).

6. Berger, L. Emission of spin waves by a magnetic multilayer traversed by a current. *Phys. Rev. B* **54,** 9353–9358 (1996).

7. Smith, N. & Arnett, P. White-noise magnetization fluctuations in magnetoresistive heads. *Appl. Phys. Lett.* **78,** 1448–1450 (2001).

8. Maat, S., Smith, N., Carey, M. J. & Childress, J. R. Suppression of spin torque noise in current perpendicular to the plane spin-valves by addition of Dy cap layers. *Appl. Phys. Lett.* **93,** 103506 (2008).

9. Tokura, Y. O. and M. I. and A. S. and T. M. and H. S. and H. A. and M. K. and Y. Tunneling Magnetoresistance above Room Temperature in La 0.7 Sr 0.3 MnO 3 /SrTiO 3 /La 0.7 Sr 0.3 MnO 3 Junctions. *Jpn. J. Appl. Phys.* **42,** L369 (2003).

10. Gomes, I. T. *et al.* Structural and magnetic characterization of LaSrMnO3 thin films deposited by laser ablation on MgO substrates. *J. Magn. Magn. Mater.* **322,** 1174–1177 (2010).

11. Ziese, M. *et al.* Tailoring Magnetic Interlayer Coupling in ${\mathrm{La}}_{0.7}{\mathrm{Sr}}_{0.3}{\mathrm{MnO}}_{3}/{\mathrm{SrRuO}}_{3}$ Superlattices. *Phys. Rev. Lett.* **104,** 167203 (2010).

12. Puli, V. S. *et al.* Structure, dielectric, ferroelectric, and energy density properties of (1 - x)BZT-xBCT ceramic capacitors for energy storage applications. *J. Mater. Sci.* 1–7 (2012). doi:10.1007/s10853-012-6990-1

13. Yokoyama, S. *et al.* Dependence of electrical properties of epitaxial Pb(Zr,Ti)O 3 thick films on crystal orientation and Zr/(Zr+Ti) ratio. *J. Appl. Phys.* **98,** (2005).

14. Page, K., Proffen, T., Niederberger, M. & Seshadri, R. Probing local dipoles and ligand structure in BaTiO3 nanoparticles. *Chem. Mater.* **22,** 4386–4391 (2010).

15. Tian, Y., Wei, L., Chao, X., Liu, Z. & Yang, Z. Phase Transition Behavior and Large Piezoelectricity Near the Morphotropic Phase Boundary of Lead-Free (Ba 0.85 Ca 0.15)(Zr 0.1 Ti 0.9)O 3 Ceramics. *J. Am. Ceram. Soc.* **96,** 496–502 (2013).

16. Wang, Z.-M. *et al.* Crystallization, phase evolution and ferroelectric properties of sol-gel-synthesized Ba(Ti0.8Zr0.2)O3-x(Ba 0.7Ca0.3)TiO3 thin films. *J. Mater. Chem. C* **1,** (2013).

17. Puli, V. S. *et al.* Barium zirconate-titanate/barium calcium-titanate ceramics via sol–gel process: novel high-energy-density capacitors. *J. Phys. D. Appl. Phys.* **44,** 395403 (2011).

18. Liu, W. & Ren, X. Large Piezoelectric Effect in Pb-Free Ceramics. *Phys. Rev. Lett.* **103,** 257602 (2009).

19. Kumar, A., Rivera, I. & Katiyar, R. S. Investigation of local structure of lead-free relaxor Ba(Ti0.70Sn0.30)O3 by Raman spectroscopy. *J. Raman Spectrosc.* **40,** 459–462 (2009).

20. Tang, X. G., Chew, K.-H. & Chan, H. L. W. Diffuse phase transition and dielectric tunability of Ba(ZryTi1−y)O3 relaxor ferroelectric ceramics. *Acta Mater.* **52,** 5177–5183 (2004).

21. Sczancoski, J. C. *et al.* Structure and optical properties of [Ba1–xY2x/3](Zr0.25Ti0.75)O3 powders. *Solid State Sci.* **12,** 1160–1167 (2010).

22. Scalabrin, A., Chaves, A. S., Shim, D. S. & Porto, S. P. S. Temperature dependence of the A1 and E optical phonons in BaTiO3. *Phys. Status Solidi* **79,** 731–742 (1977).

23. Moreira, M. L. *et al.* Hydrothermal Microwave: A New Route to Obtain Photoluminescent Crystalline BaTiO3 Nanoparticles. *Chem. Mater.* **20,** 5381–5387 (2008).

24. Use of Raman spectroscopy to determine the site occupancy of dopants in BaTiO3. *J. Appl. Phys.* **109,** 114110 (2011).

25. Pachauri, N. *et al.* (LiFe5O8) single crystals Study of structural and ferromagnetic resonance properties of spinel lithium ferrite (LiFe 5 O 8) single crystals. **233907,** 1–6 (2015).

CONCLUSIONS

I have successfully deposited heterostructure of ferroelectric BZT-BCT and ferromagnetic LSMO thin films, which shows the expected magnetoelectric coupling between them. The BZT-BCT ferroelectric thin film shows polarization switching behavior with a large remnant polarization of 93.3 $\mu C/cm^2$, a coercive field of 159.89 kV/cm, and a large dielectric constant with negligible loss. The well-behaved M-H hysteresis loop at room temperature confirms the ferromagnetic nature of all the LSMO thin films with high saturation and remnant magnetization. The observed right shift of the hysteresis loops of LSMO in presence of an FE top layer is an indication of the desired magnetoelectric coupling between the layers. Moreover, temperature dependent magnetization confirmed a high Curie temperature of 360K which was very close to the bulk sample. FMR data demonstrate that the thin films deposited on LAO substrate show the lowest linewidth offset compared to the films on Pt substrate. The Gilbert damping parameter and the gyromagnetic ratio are smaller for the thin films on LAO substrate indicating possible applications mentioned in the earlier sections such as MRAM, data storage, high-speed switching sensors, actuators etc. Moreover, the in-plane anisotropy field is much higher for the films on LAO than the films on Pt indicating strong anisotropy in LSMO/ LAO. On the other hand, the dynamic behavior of LSMO/LAO thin film is quite similar to the same thin film with the top ferroelectric layer. However, the dynamic properties of LSMO/Pt change a lot with FE top layer. So, we can conclude that LSMO thin film can be joined with another ferroelectric layer for device applications when the insulating substrate or some insulating layer is necessary for isolation.

REFERENCES

1. Martin, L. W. *et al.* Multiferroics and magnetoelectrics: thin films and nanostructures. *J. Phys. Condens. Matter* **20,** 434220 (2008).

2. Spaldin, N. A., Fiebig, M. & Mostovoy, M. The toroidal moment in condensed-matter physics and its relation to the magnetoelectric effect. *J. Phys. Condens. Matter* **20,** 434203 (2008).

3. Ederer, C. & Spaldin, N. A. Towards a microscopic theory of toroidal moments in bulk periodic crystals. *Phys. Rev. B - Condens. Matter Mater. Phys.* **76,** 1–13 (2007).

4. Hill, N. A. Why Are There so Few Magnetic Ferroelectrics? *J. Phys. Chem. B* **104,** 6694–6709 (2000).

5. Vaz, C. A. F., Hoffman, J., Ahn, C. H. & Ramesh, R. Magnetoelectric coupling effects in multiferroic complex oxide composite structures. *Adv. Mater.* **22,** 2900–2918 (2010).

6. Wang, J. *et al.* Epitaxial BiFeO$_3$ multiferroic thin film heterostructures. *Science (80-.).* **299,** 1719–1722 (2003).

7. Films, B. T. & Kim, J. W. Effects of Transition Metal Ion Doping on Structure and Electrical Properties of. (2012). doi:10.1111/j.1551-2916.2012.05081.x

8. Zhang, S. *et al.* Observation of room temperature saturated ferroelectric polarization in Dy substituted BiFeO 3 ceramics. *J. Appl. Phys.* **111,** (2012).

9. Zaghrioui, M., Grenèche, J. M., Autret-Lambert, C. & Gervais, M. Effect of Fe substitution on multiferroic hexagonal YMnO3. *J. Magn. Magn. Mater.* **323,** 509–514 (2011).

10. Kimura, T. *et al.* Magnetocapacitance effect in multiferroic <math display='inline'> <mrow> <msub> <mrow> <mi mathvariant='normal'>BiMnO</mi> </mrow> <mrow> <mn>3</mn> </mrow> </msub> </mrow> </math>. *Phys. Rev. B* **67,** 180401 (2003).

11. Kimura, T. *et al.* Magnetic control of ferroelectric polarization. *Nature* **426,** 55–58 (2003).

12. Goto, T., Kimura, T., Lawes, G., Ramirez, A. P. & Tokura, Y. Ferroelectricity and Giant Magnetocapacitance in Perovskite Rare-Earth Manganites. *Phys. Rev. Lett.* **92,** 257201 (2004).

13. Kimura, T. Magnetoelectric Hexaferrites. *Annu. Rev. Condens. Matter Phys.* **3,** 93–110 (2012).

14. Chu, Y.-H. *et al.* Electric-field control of local ferromagnetism using a magnetoelectric multiferroic. *Nat Mater* **7,** 478–482 (2008).

15. Béa, H. *et al.* Mechanisms of Exchange Bias with Multiferroic ${\mathrm{BiFeO}}_{3}$ Epitaxial Thin Films. *Phys. Rev. Lett.* **100,** 17204 (2008).

16. Shrout, T. R. & Zhang, S. J. Lead-free piezoelectric ceramics: Alternatives for PZT? *J. Electroceramics* **19,** 111–124 (2007).

17. Thakur, O. P., Prakash, C. & James, A. R. Enhanced dielectric properties in modified barium titanate ceramics through improved processing. *J. Alloys Compd.* **470,** 548–551 (2009).

18. Wang, X., Yamada, H. & Xu, C. N. Large electrostriction near the solubility limit in BaTi O3 -CaTi O3 ceramics. *Appl. Phys. Lett.* **86,** (2005).

19. Liu, W. & Ren, X. Large Piezoelectric Effect in Pb-Free Ceramics. *Phys. Rev. Lett.* **103,** 257602 (2009).

20. Li, L.-Y. & Tang, X.-G. Effect of electric field on the dielectric properties and ferroelectric phase transition of sol–gel derived (Ba0.90Ca0.10)TiO3 ceramics. *Mater. Chem. Phys.* **115,** 507–511 (2009).

21. Keeble, D. S., Benabdallah, F., Thomas, P. a., Maglione, M. & Kreisel, J. Revised structural phase diagram of (Ba0.7Ca0.3TiO3)-(BaZr0.2Ti0.8O3). *Appl. Phys. Lett.* **102,** 92903 (2013).

22. Cesaria, M., Caricato, A. P., Maruccio, G. & Martino, M. LSMO – growing opportunities by PLD and applications in spintronics. *J. Phys. Conf. Ser.* **292,** 12003 (2011).

23. Martínez-Boubeta, C. *et al.* Epitaxial Integration of La2/3Sr1/3MnO3 and Fe Films by the Use of a MgO Spacer. *Cryst. Growth Des.* **10,** 1017–1020 (2010).

24. Substrate effect on the magnetic microstructure of La0.7Sr0.3MnO3 thin films studied by magnetic force microscopy. *Appl. Phys. Lett.* **78,** 3681–3683 (2001).

25. Ishii, Y. *et al.* Perovskite manganite magnetic tunnel junctions with enhanced coercivity contrast. *Appl. Phys. Lett.* **87,** 22509 (2005).

26. Xiong, Z. H., Wu, D., Valy Vardeny, Z. & Shi, J. Giant magnetoresistance in organic spin-valves. *Nature* **427,** 821–824 (2004).

27. Berger, L. Emission of spin waves by a magnetic multilayer traversed by a current. *Phys. Rev. B* **54,** 9353–9358 (1996).

28. Smith, N. & Arnett, P. White-noise magnetization fluctuations in magnetoresistive heads. *Appl. Phys. Lett.* **78,** 1448–1450 (2001).

29. Maat, S., Smith, N., Carey, M. J. & Childress, J. R. Suppression of spin torque noise in current perpendicular to the plane spin-valves by addition of Dy cap layers. *Appl. Phys. Lett.* **93,** 103506 (2008).